First posted online on 27 January 2020 as 10.1242/dev.181420
Access the most recent version at http://dev.biologists.org/lookup/doi/10.1242/dev.181420

Optic cup morphogenesis requires neural crest-mediated basement membrane assembly

Chase D. Bryan[1], Macaulie A. Casey[1], Rebecca L. Pfeiffer[2], Bryan W. Jones[2], Kristen M. Kwan[1*]

[1] Department of Human Genetics, University of Utah, Salt Lake City, UT, USA

[2] Department of Ophthalmology and Visual Sciences, John A. Moran Eye Center, University of Utah School of Medicine, Salt Lake City, UT, USA

[*] Correspondence to: Department of Human Genetics, EIHG 5100, University of Utah Medical Center, 15 North 2030 East, Salt Lake City, UT 84112, USA.

Email address: kmkwan@genetics.utah.edu

Keywords: eye, morphogenesis, extracellular matrix, basement membrane, nidogen, neural crest

Abstract

Organogenesis requires precise interactions between a developing tissue and its environment. In vertebrates, the developing eye is surrounded by a complex extracellular matrix as well as multiple mesenchymal cell populations. Disruptions to either the matrix or periocular mesenchyme can cause defects in early eye development, yet in many cases, the underlying mechanism is unknown. Here, using multidimensional imaging and computational analyses in zebrafish, we establish that cell movements in the developing optic cup require neural crest. Ultrastructural analysis reveals that basement membrane formation around the developing eye is also dependent on neural crest, but only specifically around the retinal pigment epithelium. Neural crest cells produce the extracellular matrix protein nidogen: impairing nidogen function disrupts eye development, and strikingly, expression of nidogen in the absence of neural crest partially restores optic cup morphogenesis. These results demonstrate that eye formation is regulated in part by extrinsic control of extracellular matrix assembly.

Introduction

Vertebrate optic cup morphogenesis requires precise coordination of cell and tissue movements, which generate the shape and organization crucial for eye function (Hilfer, 1983; Schmitt and Dowling, 1994; Schook, 1980; Walls, 1942). Initially, the optic vesicles evaginate from the developing forebrain; the bilayered vesicles will give rise to neural retina and retinal pigment epithelium (RPE). The optic vesicles elongate and their connection to the brain narrows, generating the optic stalk. During invagination, the final stage of optic cup morphogenesis, the optic vesicles bend, become hemispherical, and enwrap the lens as it arises from the overlying ectoderm, while the optic fissure forms along the ventral surface of the optic cup and optic stalk. In zebrafish, optic cup morphogenesis occurs rapidly, 10-24 hours post fertilization (hpf). Lineage tracing and live imaging, especially in recent work in zebrafish, has enabled detailed analyses of cell movements during eye development, including identification of extended evagination and rim movement (Heermann et al., 2015; Kwan et al., 2012; Li et al., 2000; Picker et al., 2009; Sidhaye and Norden, 2017). Rim movement occurs during invagination: a subset of cells from the medial layer of the optic vesicle moves around the rim of the vesicle and contributes to the lateral layer, the prospective neural retina. Cells remaining in the medial layer flatten and comprise the RPE. However, the molecular mechanisms governing rim movement and invagination are only partly understood; much work remains to be done to identify extrinsic cues regulating these dramatic cell movements and changes in morphology. Two potential sources of such extrinsic cues are the extracellular matrix (ECM) and nearby cell populations.

The ECM, a crucial regulator of cell adhesion, migration, and survival, is implicated in the morphogenesis of many tissues. ECMs are dynamic scaffolds whose components dictate their function with respect to adhesion, rigidity, growth factor presentation, and many other biological processes, but how ECM structures are built and remodeled *in vivo* is not

well understood. A complex ECM has long been known to surround the optic vesicle throughout optic cup morphogenesis (Dong and Chung, 1991; Hendrix and Zwaan, 1975; Kwan, 2014; Peterson et al., 1995; Svoboda and O'Shea, 1987; Tuckett and Morriss-Kay, 1986), yet the dynamics of ECM assembly around the developing eye are poorly understood. Only recently have molecular roles of fibronectin and laminin during optic cup morphogenesis been elucidated (Bryan et al., 2016; Hayes et al., 2012; Huang et al., 2011; Ivanovitch et al., 2013; Sidhaye and Norden, 2017); the roles of many other ECM proteins during optic cup morphogenesis are unknown, as are the functions of specialized ECM structures such as basement membranes (BM).

The periocular mesenchyme (POM), a heterogeneous cell population comprised of neural crest and mesodermally-derived mesenchyme, is found in close proximity to the optic cup (Johnston et al., 1979), and multiple tissues in the mature eye are derived in part from these mesenchymal cells (Williams and Bohnsack, 2015). Mesenchymal cells are known to influence the morphogenesis of many epithelial organs through growth factor signaling as well as modifications to the surrounding ECM (Grocott et al., 2011; Nelson and Larsen, 2015; Thesleff, 2003; Wells et al., 2013). Mutations to transcription factors affecting POM development or survival (e.g. *ap2a*, *pitx2* or *zic2*) cause severe optic cup malformations (Bassett et al., 2010; Bohnsack et al., 2012; Gestri et al., 2009; Li and Cornell, 2007; Sedykh et al., 2017), and recent work indicated a role for POM later during optic fissure closure (Gestri et al., 2018). Together these data suggest a crucial role for the POM in regulating optic cup morphogenesis.

Here, we sought to determine how eye morphogenesis is regulated by a specific subpopulation of the POM, the neural crest. We find that optic cup formation is impaired in mutants exhibiting a severe loss of neural crest, and 4-dimensional timelapse imaging demonstrates neural crest cells migrate around the eye during optic cup morphogenesis. We

pinpoint specific ocular cell movements that are dependent on neural crest: rim movements driving optic cup invagination and RPE cell movements are disrupted in the absence of neural crest. Because mesenchymal cells can act on epithelial organs by modifying the ECM, we use transmission electron microscopy to visualize ECM ultrastructure: in the absence of neural crest, the BM around the eye is disrupted specifically around the RPE. Finally, we uncover a key molecular effector of neural crest interaction with the eye: optic cup morphogenesis is dependent upon nidogens, modulators of ECM assembly, deposited by neural crest cells. Overall, our results reveal how the eye and surrounding tissues cooperate to generate specific ECM structures, which in turn are essential for proper morphogenesis.

Results

Optic cup morphogenesis requires neural crest

Previous studies have revealed crosstalk between the developing eye and the neural crest (Bassett et al., 2010; Bohnsack et al., 2012; Eberhart et al., 2008; Grocott et al., 2011; Langenberg et al., 2008; Sedykh et al., 2017), yet we do not understand, from the ocular perspective, what specific aspects of eye development and morphogenesis require this extrinsic cell population. We therefore set out to examine eye morphogenesis in the zebrafish *tfap2a*^{ts213}*;foxd3*^{zdf10} double mutant, which displays a near-complete loss of neural crest (Arduini et al., 2009; Wang et al., 2011).

At 24 hpf, *tfap2a;foxd3* double mutants display gross morphological defects in optic cup invagination and optic fissure formation. At the dorsal-ventral midpoint of the optic cup, the nasal side of the neural retina is flatter than sibling controls and fails to completely enwrap the lens (Fig 1A-B). Quantification of optic cup invagination angle reveals a decrease in the extent to which the retina enwraps the lens in *tfap2a;foxd3* mutants (37.8±1.9°) compared to wildtype controls (47.3±1.8°; Fig 1G). The optic fissure, a cleft structure at the

ventral side of the optic stalk and optic cup, does not form correctly in *tfap2a;foxd3* mutants: control embryos display two closely apposed fissure margins with an opening angle of 16.9±1.9°, while the optic fissure opening in *tfap2a;foxd3* mutants is larger (33.8±3.1°; Fig 1C-D, H). Importantly, compared to controls, we find very few *sox10:memRFP*$^{+}$ neural crest cells adjacent to the optic cup in *tfap2a;foxd3* double mutants (Fig 1E-F). In comparison, *tfap2a* and *foxd3* single mutants display impaired optic fissure formation and decreased neural crest especially around the ventral portion of the eye (Fig S1D-E, G-H). However, neither single mutant displays as severe an effect on invagination angle or optic fissure opening angle as the *tfap2a;foxd3* double mutant (Fig S1J-K), likely due to the presence of more neural crest cells.

We also assayed optic cup development in *alyron*^{z24} (*paf1*) mutants in which neural crest development is severely impaired in an independent manner (Cretekos and Grunwald, 1999). Invagination is more severely disrupted in *paf1* mutants (25.6±3.6°) compared to wildtype controls or *tfap2a;foxd3* double mutants (Fig S1C, J). Optic fissure formation was so severely affected that optic fissure margins could not be defined, nor measured (Fig S1F). Similar to the *tfap2a;foxd3* mutants, *sox10:memRFP*$^{+}$ cells surrounding the eyes of *paf1* mutants are substantially reduced at 24 hpf (Fig S1I; Fig 1F). However, as *paf1* is expressed ubiquitously (Nguyen et al., 2010; Thisse and Thisse, 2004), despite a severe loss of neural crest, it is possible that *paf1* also plays an intrinsic role in optic cup development. Thus, further analysis of neural crest function in optic cup morphogenesis was carried out solely on *tfap2a;foxd3* double mutants.

Previous studies have suggested a role for POM in optic fissure closure (Gestri et al., 2018; Hero, 1990; Hero et al., 1991; James et al., 2016; Lupo et al., 2011; Weiss et al., 2012). Consistent with these data, most *tfap2a;foxd3* double mutants harbor optic fissure defects and gaps in ocular pigmentation (indicative of coloboma) at 52 hpf (59.38% vs 7.62% of control

embryos; Fig S1L-M). Although these previous studies have focused largely on optic fissure fusion, which occurs after optic cup morphogenesis, our observations at 24 hpf demonstrate that earlier stages of optic cup morphogenesis are also dependent upon neural crest.

The developing eye is in close proximity to neural crest throughout optic cup morphogenesis

In zebrafish, optic cup morphogenesis occurs 10-24 hours post fertilization (hpf), during which time the optic vesicles evaginate and undergo stereotypical movements and shape changes to become the organized optic cup, comprised of neural retina, retinal pigment epithelium (RPE), and lens. Neural crest cells have previously been observed migrating near the eye during these stages of optic cup morphogenesis, but the extent of the interactions between these tissues is unknown (Gestri et al., 2018; Langenberg et al., 2008). To determine how optic cup morphogenesis might be influenced by neural crest, we first asked when and where these cells interact with the developing eye. To visualize both the eye and neural crest, we used double transgenic *Tg(bactin2:EGFP-CAAX)*^{z200}*;Tg(sox10:memRFP)*^{vu234} zebrafish in which GFP labels all cell membranes and RFP labels neural crest cell membranes (Gordon et al., 2018; Kirby et al., 2006). We performed 4-dimensional timelapse imaging of optic cup morphogenesis (12.5-24.5 hpf; Fig 1I-L', Movies 1, 2). At the start of our imaging, neural crest cells have made contact with the posterior margin of the optic vesicle (Fig 1I, I'). As the optic vesicle elongates, neural crest cells migrate anteriorly between the prospective brain and optic vesicle, around to the nasal margin of the optic vesicle (Fig 1J, J'; Movie 1), then enwrap the optic stalk (Fig 1J', Movie 2). During invagination, neural crest cells migrate laterally and ventrally to surround the posterior and ventral optic cup, and appear to be in close contact with the eye, more so than the prospective brain (Fig 1K, K'). By 24.5 hpf, when the optic fissure has formed, neural crest is moving through the fissure into the space

between the neural retina and lens (Fig 1L', *arrow*). By the end of the process, the RPE side of the optic cup is encapsulated by neural crest (Fig 1L).

Retina and RPE cell movements require neural crest

Due to the morphological defects in the nasal and ventral optic cup in *tfap2a;foxd3* double mutants, we initially hypothesized that optic cup patterning might depend upon neural crest. Antibody staining for Pax2a, a transcription factor expressed in the ventral optic cup and optic stalk (Fig S2A), reveals that Pax2a expression is expanded dorsally and temporally in *tfap2a;foxd3* mutants (Fig S2D, D', I; 134.2±10.5° compared to 100.3±5.9° in sibling controls), but interestingly, only in the RPE layer (Fig S2D, D', *arrowheads*). This was observed in *tfap2a;foxd3* double mutants as well as *tfap2a* and *foxd3* single mutants (Fig S2B-C). In other models of optic cup mispatterning, Pax2a is expanded not just into the RPE layer but throughout the ventral retina (Lee et al., 2008; Sedykh et al., 2017). The *tfap2a;foxd3* mutant phenotype is distinct in its restriction to the RPE layer, and suggests that cell movements may be disrupted.

We hypothesized that specific optic cup morphogenetic movements are dependent on neural crest; uncovering these would allow us to pinpoint the cellular basis of eye defects in the absence of neural crest, and also identify specific regions of the eye where neural crest might influence development. Based on the gross morphological phenotype and Pax2a localization, we suspected that rim movement might be disrupted in *tfap2a;foxd3* mutants. During invagination, a subset of cells executes rim movement, moving from the medial layer around the rim of the developing optic cup into the lateral layer to contribute to neural retina (Heermann et al., 2015; Kwan et al., 2012; Picker et al., 2009; Sidhaye and Norden, 2017). The expanded Pax2a expression we observed could result from failure of $Pax2a^{+}$ cells to undergo rim movement into the neural retina, thus remaining in the apparent RPE layer. In

addition, we hypothesized that RPE cell movements might also depend on neural crest, given their proximity throughout optic cup morphogenesis (Fig 1I-L). To determine if specific regional eye cell movements are neural crest-dependent, we performed live imaging of optic cup morphogenesis in wildtype and *tfap2a;foxd3* mutant embryos followed by 4-dimensional cell tracking using LongTracker (Kwan et al., 2012) and quantitative analysis of 3D speed and 3D trajectory (Fig 2, Movie 3).

We first examined movements of nasal retina and RPE cells since we saw gross morphological defects in the nasal hemisphere of *tfap2a;foxd3* double mutant eyes. We selected these cells from their final positions at 24 hpf in double mutant and wildtype data sets (Gordon et al., 2018), and tracked these cells retrospectively to establish their origins and movements from optic vesicle stage; a subset of cells and trajectories is shown (Fig 2). Nasal retina cells originate from a similar location in wildtype and *tfap2a;foxd3* mutants (Fig 2C-D, Movies 4, 5). Trajectory shape is similar, but timing is altered: wildtype cells turn away from the midline ~17.75 hpf, however, that turn is delayed in *tfap2a;foxd3* mutants until ~19.5 hpf (Movies 4, 5). Quantification of these movements in 3 dimensions (Fig 2K-M) reveals that nasal retina cells unexpectedly move faster and farther in *tfap2a;foxd3* mutants (avg. speed 0.60±0.04 μm/min; total dist. 402.80±17.33 μm) than wildtypes (avg. speed 0.53±0.03 μm/min; total dist. 352.41±29.99 μm; Fig 2K-L), although net displacement is unchanged (wildtype 111.55±18.18 μm; *tfap2a;foxd3* 124.08±8.43 μm; Fig 2M). Nasal RPE cell movements are also altered in *tfap2a;foxd3* mutants. These cells originate from the same domain in wildtype and mutant embryos, but trajectory shape is altered: wildtype nasal RPE cells move along an arc-like trajectory to the nasal RPE margin, however, *tfap2a;foxd3* mutant nasal RPE cells travel along a straight anterior path until 19.5 hpf, when they make a sudden 90° turn toward the optic cup margin (Fig 2E-F, Movies 6, 7). As with the nasal retina, nasal RPE cells move faster and farther in *tfap2a;foxd3* mutants (avg. speed 0.57±0.02

μm/min; total dist. 385.75±15.71 μm) than in wildtypes (avg. speed 0.45±0.05 μm/min; total dist. 303.01±34.06 μm; Fig 2K-L). Additionally, net displacement of nasal RPE cells is increased in *tfap2a;foxd3* mutants (170.76±14.55 μm) compared to wildtypes (131.17±10.16 μm; Fig 2M). These data suggest that cell motility within the nasal optic cup is restricted by neural crest; without nearby neural crest, cells in the nasal retina and RPE move faster and farther and with incorrect timing.

Although we did not see obvious morphological abnormalities on the temporal side of the eye in *tfap2a;foxd3* double mutants, we wondered if cell movements here might also be defective; this region of the eye is the first to contact neural crest (Fig 1). In wildtype embryos, temporal retina cells exhibiting rim movement travel around the optic cup rim starting ~20 hpf (Fig 2G, Movie 8). In *tfap2a;foxd3* mutants, equivalent cells do not initiate rim movement until ~22 hpf (Fig 2H, Movie 9). As with nasal retina cells, the 3D speeds and distances are increased in *tfap2a;foxd3* mutants (avg. speed 0.57±0.04 μm/min; total dist. 375.01±27.53 μm) compared to wildtypes (avg. speed 0.52±0.01 μm/min; total dist. 341.35±12.86 μm; Fig 2K-L), while net displacement remains unchanged (wildtype 78.50±15.07 μm; *tfap2a;foxd3* 71.48±20.79 μm; Fig 2M). We also examined temporal RPE cells, which are close to neural crest throughout most of optic cup morphogenesis. Temporal RPE cell trajectories appear similar between wildtype and *tfap2a;foxd3* mutants (Fig 2I-J, Movies 10, 11), however, cell motility is again altered. Similar to the temporal retina, temporal RPE cells move faster and farther in *tfap2a;foxd3* mutants (avg. speed 0.58±0.02 μm/min; total dist. 372.07±16.21 μm) compared to wildtypes (avg. speed 0.48±0.03 μm/min; total dist. 309.06±18.20 μm; Fig 2K-L). Unlike the nasal RPE, net displacement is unchanged for temporal RPE cells (wildtype 97.69±14.15 μm; *tfap2a;foxd3* 104.88±19.83 μm; Fig 2M). Despite a lack of gross morphological defects in the temporal optic cup in *tfap2a;foxd3* mutants, cell tracking uncovers abnormal temporal retina and RPE cell movements.

The medial side of the developing optic cup, which is in close proximity to neural crest, gives rise to RPE and nasal and temporal retina margins. Taken together, we find that cell movements executed by these different eye domains are abnormal when neural crest is lost. Specifically, 3D cell speed and distance traveled are altered: cells move faster and farther in the absence of neural crest. Additionally, the defects in nasal and temporal rim movement in *tfap2a;foxd3* double mutants may explain the Pax2a expansion into the RPE. We conclude that cell movements in the optic cup require neural crest, and their disruption in *tfap2a;foxd3* mutants results in impaired RPE and rim movement.

Basement membrane formation is disrupted specifically around the RPE in *tfap2a;foxd3* mutants

Having demonstrated a role for neural crest in regulating cell movements, we sought to determine the underlying mechanism by which neural crest influences the eye. Previous work suggested that POM signals to the developing eye via TGF-β ligands (Fuhrmann et al., 2000; Grocott et al., 2011). Using an antibody against phospho-Smad3 to detect sites of active TGF-β signaling, we asked whether loss of neural crest alters TGF-β signaling within the optic cup. We did not, however, detect any differences in phospho-Smad3 localization between control and *tfap2a;foxd3* mutant eyes, suggesting that neural crest is dispensable for TGF-β signaling in the zebrafish optic cup at 24 hpf (Fig S2E-H, quantified in Fig S2J-K).

Data from other organ systems demonstrate that mesenchymal cells can regulate epithelial morphogenesis via modifications to the ECM. We therefore asked if periocular ECM might be defective when neural crest is lost. Laminin-1 and fibronectin appear unaltered between wildtypes and *tfap2a;foxd3* double mutants (Fig S3, quantified in Fig S3I-J). Despite these core ECM components being present, mesenchymal cells can also regulate the ECM via assembly of matrices into a basement membrane (BM). Using transmission

electron microscopy, we directly visualized BMs at the basal surfaces of the brain, RPE, neural retina, and lens in 24 hpf wildtypes and *tfap2a;foxd3* mutants (Fig 3A-B). The BM lines the dark plasma membrane, and appears as a thin, contiguous surface comprised of the lighter and thicker lamina lucida and darker, thin lamina densa (Bader et al., 2013; Feitosa et al., 2011; Yurchenco and Schittny, 1990). We observe a well-defined BM lining the brain in both *tfap2a;foxd3* double mutants and control embryos; BM covers the brain over ~91% in control and ~86% in *tfap2a;foxd3* double mutants (Fig 3C-D, L). The BMs lining the neural retina and lens (Fig 3G-J), a region in which no neural crest migrates during this process, also appear intact in *tfap2a;foxd3* mutants compared to wildtype controls, with BM covering ~85% of the retina and ~88% of the lens in controls, and ~78% of the retina and 78% of the lens in *tfap2a;foxd3* double mutants (Fig 3L). In contrast, the BM surrounding the RPE is defective in *tfap2a;foxd3* double mutants (Fig 3F, F', *arrows*): in *tfap2a;foxd3* mutants, only ~45% of the RPE displays a BM with both lamina lucida and lamina densa discernable, while controls display ~91% coverage by BM (*arrowheads* in Fig 3E, E', L). Given that neural crest is in close proximity to the developing RPE throughout eye morphogenesis and no other BMs around the eye are disrupted in *tfap2a;foxd3* mutants, these results suggest that neural crest contributes to BM development or stability specifically around the RPE. To our knowledge, this is the first indication that neural crest influences the BM around the developing eye, and this may represent a novel mechanism for regulating eye morphogenesis.

The basement membrane protein nidogen is produced in part by neural crest and is decreased in *tfap2a;foxd3* mutants

To understand the underlying cause of BM disruption around the RPE in the *tfap2a;foxd3* double mutant, we set out to identify individual ECM components that might be affected. Nidogen is an ECM crosslinking protein crucial for BM assembly (Ho et al., 2008)

and, together with laminin-1, is capable of supporting embryonic-stem-cell-derived optic cup morphogenesis *in vitro* (Eiraku et al., 2011). Nidogen, provided by mesenchymal cells, is necessary for mouse lung and kidney epithelial morphogenesis (Bader et al., 2005; Ekblom et al., 1994; Kadoya et al., 1997; Willem et al., 2002). Nidogen expression is found in mouse POM and invaginating lens (Dong and Chung, 1991), and zebrafish data suggest that *nidogen 1a (nid1a), nidogen 1b (nid1b)* and *nidogen 2a (nid2a)* are expressed near the eye during optic cup morphogenesis (Carrara et al., 2019; Kudoh et al., 2001; Thisse and Thisse, 2004; Zhu et al., 2017). First, we performed our own whole mount *in situ* hybridization for the four zebrafish *nidogen* genes (Fig S4); at these stages, *nid1a* is expressed primarily in developing somites (Fig S4A, E, I), while *nid2b* is detected diffusely throughout the head at a low level (Fig S4D, H, L). In contrast, *nid1b* and *nid2a* are expressed in a pattern suggestive of POM (Fig S4B-C, F-G, J-K). Because these specific periocular cell populations are not clearly defined in whole mount *in situ* hybridization, we visualized expression of the *nidogen* genes at cellular resolution. Fluorescence *in situ* hybridization in *Tg(sox10:GFP)*^{ba4} transgenics (Dutton et al., 2008) reveals that both *nid1b* and *nid2a* are expressed by *sox10:GFP*$^{+}$ neural crest cells around the developing optic cup at 18 and 24 hpf (Fig 4A-D and insets). *nid1b* and *nid2a* are also expressed in the ectoderm and developing lens at these timepoints, but notably appear to be absent in the neural retina and RPE.

As confirmation that nidogens are produced by neural crest, we examined nidogen-1 protein localization around the eye, and whether its deposition is reduced in *tfap2a;foxd3* double mutants; although we tested nidogen-2 antibodies in zebrafish, we were unable to achieve specific staining, so our analysis is limited to nidogen-1. In 24 hpf wildtype embryos, nidogen-1 protein is found at basal surfaces surrounding the RPE, neural retina, and lens (Fig 4E-E"), consistent with localization to BMs around the eye, as well as the brain. Nidogen-1 protein is found deposited along a similar percentage of brain and lens surface in

tfap2a;foxd3 mutants (brain ~86.0%, lens ~71.2%) and wildtype siblings (brain ~85.2%, lens ~77.8%; Fig 4G), but is diminished around the RPE of *tfap2a;foxd3* mutants (Fig 4F-G). While nidogen lines an average of 88.4% of the RPE surface in 24 hpf wildtype embryos, only ~64.7% of the RPE is lined in *tfap2a;foxd3* mutants. Notably, much of the nidogen signal surrounding the RPE in the double mutant is found closer to the nasal and temporal margins of the optic cup, where the RPE is in close proximity to the olfactory placode and surface ectoderm, respectively, other sources of nidogen production (Fig 4F). Taken together, these data suggest that neural crest produces a portion of the nidogen around the RPE, and thus we hypothesize that BM assembly around the eye is a multi-tissue process: nidogen, partially supplied by neural crest, may be necessary for BM assembly specifically around the RPE.

Dominant-interfering nidogen disrupts optic cup morphogenesis

The discontinuous BM we observe around the RPE in the *tfap2a;foxd3* double mutant was reminiscent of BM alterations found when Nidogen is disrupted (genetically or functionally) in mouse lung and kidney morphogenesis (Bader et al., 2005; Ekblom et al., 1994; Kadoya et al., 1997; Willem et al., 2002). This observation, coupled with the finding that *nid1b* and *nid2a* are expressed by neural crest cells, suggested a potential functional role for nidogen in optic cup morphogenesis which we set out to test.

Since multiple *nidogens* are expressed in the neural crest and head during eye development, we initially took a dominant-interference strategy to disrupt nidogen function. We used Nd-III, an internal deletion form of mouse Nidogen-1 lacking domains required for binding collagen IV and heparin sulfate proteoglycan, but retaining the laminin binding domain (Fox et al., 1991; Reinhardt et al., 1993). *In vitro* characterization demonstrated that Nd-III acts in a dominant-inhibitory fashion by competitively preventing full-length Nidogen

from binding to laminin, thereby blocking bridging of laminin to other ECM components (Pujuguet et al., 2000). Zebrafish nidogen-1a is most closely related to mouse Nidogen-1, thus we generated stable transgenic zebrafish lines expressing either full-length zebrafish *nid1a* (Fig 5A, WT-Nid1a), or dominant inhibitory *nid1a* based on the Nd-III fragment (Fig 5A, DI-Nid1a). By using heat-shock inducible transgenes, we were able to both temporally control expression of WT-Nid1a or DI-Nid1a and detect transgene expression via the lyn-mCherry reporter (Fig 5A).

We observed neural crest cells contacting the optic vesicle at 12.5 hpf (Fig 1I), therefore we heat shocked at 12-13 hpf to induce WT-Nid1a or DI-Nid1a expression at the onset of neural crest migration around the optic vesicle. We examined optic cups of *Tg(bactin2:EGFP-CAAX)* zebrafish double transgenic for *Tg(hs:WT-Nid1a)* or *Tg(hs:DI-Nid1a)* (Fig 5B-D). Ubiquitous overexpression of WT-Nid1a slightly but significantly impairs invagination (42.3±1.7° vs 46.8±1.4° in controls), optic fissure formation (25.7±2.6° vs 16.3±2.5° in controls, Fig 5C-C', G-H), and lens morphogenesis, resulting in a slightly ovoid lens (Fig 5I). However, DI-Nid1a overexpression substantially impairs optic cup morphogenesis, including invagination (32.3±1.5°), optic fissure formation (44.5±3.4°), and lens morphogenesis (Fig 5D-D', G-I). This is consistent with a recent study using morpholinos and RNA injection of an inferred dominant-negative form of Nidogen-1b (Carrara et al., 2019). Because such dramatic phenotypes could be due to indirect effects on neural crest migration, we visualized neural crest in the *sox10:GFP* transgenic line when either WT-Nid1a or DI-Nid1a is overexpressed (Fig 5E-F). As neural crest cells migrate into the optic fissure near the end of optic cup morphogenesis (Fig 1L'), we quantified the number of GFP^+ cells in contact with the optic fissure at 24 hpf as a measure of migration. We find that heat shock-induced overexpression of WT-Nid1a or DI-Nid1a does not affect neural

crest migration (Fig 5J) and therefore conclude that DI-Nid1a impairs optic cup morphogenesis through direct effects on the eye.

Nidogen overexpression partially rescues *tfap2a;foxd3* mutant optic cup phenotypes

Nidogen expression in the neural crest, coupled with phenotypes observed when DI-Nid1a is overexpressed, suggested that disruptions to nidogen's matrix-bridging function might underlie the eye morphogenesis defects in *tfap2a;foxd3* double mutants. We therefore asked whether those defects might be due to a lack of nidogen deposited by neural crest, and whether we might be able to rescue aspects of eye morphogenesis by providing nidogen.

To test this, we used our heat-shock inducible transgenic to ubiquitously overexpress WT-Nid1a in *tfap2a;foxd3* double mutants, where there would be no neural crest present around the RPE to produce nidogen. We generated *Tg(bactin2:EGFP-CAAX);Tg(hs:WT-Nid1a)* double transgenic *tfap2a;foxd3* double mutants, to visualize optic cups of control (non-heat shocked) and heat-shocked embryos. Control *tfap2a;foxd3* mutants, as expected, exhibit retinal invagination and optic fissure formation defects (Fig 6A-B', E-F). As described (Fig 5), overexpression of WT-Nid1a in wildtypes slightly impairs invagination, optic fissure formation, and lens morphogenesis (Fig 6C-C', E-G). Upon WT-Nid1a overexpression in *tfap2a;foxd3* double mutant embryos, mutant phenotypes appear partially rescued: the nasal retina more fully enwraps the lens and the optic fissure margins are more closely set (Fig 6D-D', E-G). Quantification reveals that WT-Nid1a overexpression improves invagination angle (39.9±1.8° vs 36.8±1.6° in control double mutants; Fig 6E) and optic fissure formation (25.1±2.4° vs 33.0±3.5° in control double mutants; Fig 6F). The phenotype of heat shocked mutant embryos is very similar to heat shocked wildtype embryos, with no statistical difference in invagination angle (wildtype 39.6±0.7°; *tfap2a;foxd3* 39.9±1.8°; Fig 6E) or optic fissure angle (wildtype 25.3±1.6°; *tfap2a;foxd3* 25.1±2.4°; Fig 6F). Lenses in

both genotypes are similarly affected, becoming ovoid (Fig 6G). These data suggest that ubiquitously expressing nidogen can partially rescue optic cup morphogenesis in the absence of neural crest. Despite this, our observation of the overexpression phenotype, as opposed to a full rescue, was slightly concerning as it demonstrated that ectopic nidogen can interfere with optic cup morphogenesis, but did not fully establish whether it plays a vital role in the process.

Nidogen is necessary for optic cup morphogenesis

While our previous experiments suggested that neural crest-derived nidogen might play a role in optic cup morphogenesis, we sought to determine whether endogenous nidogen is necessary. Because we detected *nid1b* and *nid2a* transcripts in neural crest cells around the developing eye, we assayed *nid1b*^{sa13713} splice site and *nid2a*^{sa15802} premature stop mutants as single and zygotic double mutants but found no obvious optic cup defects (data not shown). *nid1b;nid2a* double mutants are adult viable and fertile, therefore, we also assayed optic cup morphogenesis in maternal-zygotic (MZ) *nid1b;nid2a* double mutant embryos. Whole mount *in situ* hybridization suggests that both genes are down-regulated or absent in the cranial neural crest (and other tissues) of *MZnid1b;MZnid2a* mutants compared to control embryos (Fig 7B-C, F-G), and antibody staining revealed a dramatic reduction in BM-localized nidogen-1 (Fig S5), confirming the specificity of the antibody. However, to our surprise, *MZnid1b;MZnid2a* mutant eyes are phenotypically indistinguishable from controls at 24 hpf (Fig 7I-J, M-N, Q-R, V-X). As nidogen proteins can function redundantly in the BM (Salmivirta et al., 2002), compensation by other *nidogen* genes might phenotypically mask loss of *nid1b* and *nid2a* during optic cup development, as previously observed in mouse and zebrafish *nidogen* single mutants (Bader et al., 2005; Böse et al., 2006; Zhu et al., 2017). In certain mutants, compensatory upregulation of closely related transcripts may be a common

phenomenon (El-Brolosy et al., 2019). Using *in situ* hybridization and RT-qPCR (Fig 7A-H, U), expression of other *nidogens* is altered in *MZnid1b;MZnid2a* mutants: *nid2b* transcripts are upregulated nearly three times wildtype levels in *MZnid1b;MZnid2a* mutants, while, somewhat surprisingly, *nid1a* mRNA levels are decreased. Thus, we hypothesize that compensatory upregulation of *nid2b* could be sufficient to support optic cup morphogenesis in the absence of *nid1b* and *nid2a*.

To test this, we used CRISPR/Cas9 mutagenesis to generate transient *nid1a;nid2b* mutants (crispants) in the *MZnid1b;MZnid2a* background, for a putative quadruple mutant. We targeted both *nid1a* and *nid2b* to avoid compensation by any functional *nidogen* genes, and targeted *golden* (*slc24a5*) as an independent control locus (Fig 7I-T; Hoshijima et al., 2016). We find that *nidogen* crispants phenocopy *tfap2a;foxd3* double mutants (Fig 7L, P, T): invagination is impaired in *nidogen* crispants (41.6±1.2°) compared to uninjected (44.6±1.5°) or *golden* crispant controls (46.3±0.9°; Fig 7V), and optic fissure formation is disrupted in *nidogen* crispants (33.7±3.7°) versus uninjected (19.9±2.1°) or *golden* crispant controls (20.1±1.8°; Fig 7W). Nidogen does not appear to be necessary for neural crest migration or survival, as *sox10:memRFP*$^{+}$ cells still surround the RPE in *nidogen* crispants (Fig 7T), as in uninjected or *golden* crispant controls (Fig 7R-S), suggesting that loss of nidogen directly affects optic cup morphogenesis, rather than a secondary effect due to impairing neural crest. Contrary to DI-Nid1a overexpression, *nidogen* crispants do not display lens morphogenesis defects at 24 hpf (Fig 7L, X), suggesting that genetic disruption of all *nidogens* impairs ECM assembly and morphogenesis differently than DI-Nid1a. Together, these results demonstrate that nidogen is a crucial component of the ECM required to support multiple aspects of optic cup morphogenesis, and loss of nidogens phenocopies loss of neural crest.

Discussion

Here, we demonstrate that early eye morphogenesis requires neural crest, and present a working model in Fig 8. The zebrafish *tfap2a;foxd3* double mutant, in which neural crest is genetically disrupted (Arduini et al., 2009; Wang et al., 2011), exhibits aberrant invagination cell movements and discontinuous, disrupted basement membranes, specifically around the developing RPE. We identify the matrix bridging protein nidogen as a key component of the periocular ECM which is provided in part by neural crest; disruptions to nidogen function impair optic cup morphogenesis.

Mesenchymal regulation of epithelial morphogenesis

Developing epithelia of the lung, kidney, salivary gland, and tooth require mesenchymal interactions to acquire their mature, functional structures (Bader et al., 2005; Ekblom et al., 1994; Kadoya et al., 1997; Thesleff, 2003). Prior work has implicated mesenchyme in eye development: disruptions to POM cause profound optic cup morphogenetic defects (Bassett et al., 2010; Lupo et al., 2011). While POM has long been observed in close proximity to the developing optic cup, the POM is a heterogeneous mix of neural crest and mesodermally-derived mesenchymal cells (Gage et al., 2005; Johnston et al., 1979), and specific molecular contributions from either tissue during early eye development are not well understood.

Several signaling pathways crucial for eye development are regulated in part by POM, including Hh, TGF-β, and Wnt (Fuhrmann et al., 2000; Grocott et al., 2011; Sedykh et al., 2017), thus neural crest cells could drive optic cup morphogenesis by modulating morphogen signaling. However, in zebrafish *tfap2a;foxd3* mutants, Pax2a expression is not expanded in a manner consistent with aberrant Hh signaling (Gordon et al., 2018; Lee et al., 2008; Sedykh et al., 2017), nor is TGF-β signaling altered. The remaining mesodermal mesenchyme may be

sufficient for proper Hh and TGF-β signaling in zebrafish; additional studies will be necessary to dissect specific roles of mesodermal mesenchyme during optic cup morphogenesis.

Eye morphogenesis requires neural crest-mediated ECM assembly

The periocular ECM plays key roles in optic cup morphogenesis. In retinal organoid culture, the exogenous components (beyond media) to elicit optic cup morphogenesis are nodal (a TGF-β ligand) and the ECM components laminin-1 and nidogen (Eiraku et al., 2011). Laminin is required for cell survival, apicobasal polarity and cell movements (Bryan et al., 2016; Ivanovitch et al., 2013; Nicolás-Pérez et al., 2016; Sidhaye and Norden, 2017), and fibronectin is crucial for lens formation (Hayes et al., 2012; Huang et al., 2011). Individual ECM components may each regulate specific, non-overlapping aspects of eye morphogenesis.

The dynamics of ECM deposition and assembly may be crucial for regulating cell movements. Using electron microscopy, we uncovered a loss of BM integrity specifically around the RPE in the *tfap2a;foxd3* double mutant, although major ECM components such as laminin and fibronectin are still present. Comparison of this phenotype to the *laminin-α1* mutant reinforces the functional specificity of BM molecules: loss of laminin leads to dramatically disrupted tissue polarity and cell death in the prospective RPE (Bryan et al., 2016), yet loss of RPE BM does not. Instead, the assembled BM may serve as a scaffold which enables efficient cell movements and RPE flattening, or as a dynamic substrate which provides mechanical signaling. The Hippo signaling pathway is a major cellular mechanotransducer which can respond to ECM stiffness (Chakraborty et al., 2017), and RPE development requires Yap and Taz, transcriptional coactivators of the Hippo pathway (Miesfeld et al., 2015). Although RPE differentiation appears normal without assembled BM

in the *tfap2a;foxd3* mutant (Fig S1O-P), it is an intriguing possibility that Hippo signaling could serve as a molecular link between the BM and morphogenetic movements.

Nidogens are widespread components of BMs (Ho et al., 2008) and while epithelial morphogenesis of the lung and kidney depend on nidogen, the surrounding mesenchyme is those tissues' sole source of nidogens (Bader et al., 2005; Ekblom et al., 1994; Kadoya et al., 1997; Senior et al., 1996). Here, we find that neural crest cells around the RPE produce nidogen; preventing nidogen production through loss of neural crest cells or disrupting nidogen function via expression of a dominant-interfering form of Nid1a or CRISPR/Cas9 mutagenesis impairs optic cup morphogenesis.

It has been reported that loss of the nidogen-binding site in mouse laminin-γ1 results in a higher penetrance of renal defects than loss of both nidogen 1 and 2 (Bader et al., 2005; Willem et al., 2002). This was thought to be due to an increase in free nidogen (unbound to laminin), which could act as a dominant-negative and interfere with proper matrix assembly. This may explain why ubiquitous overexpression of full-length Nid1a also causes slight defects in optic cup morphogenesis, and suggests that an optimal level of nidogen is required for proper BM architecture. While nidogen is primarily thought to crosslink laminin with collagen IV, it can also bind other components of the BM such as heparan sulfate proteoglycans and fibulin (Kalluri, 2003; Lössl et al., 2014; Pozzi et al., 2017); we do not yet fully grasp the molecular underpinnings of BM disruption when nidogen function is impaired. Moving forward, studies of other nidogen binding partners in eye development will be crucial.

Both laminin and fibronectin are still found around the RPE in the absence of neural crest cells, but BM integrity at this site is significantly disrupted. Proper ECM interactions regulate many aspects of eye development including rim movement (Bryan et al., 2016; Martinez-Morales et al., 2009; Sidhaye and Norden, 2017), a process we show to be disrupted

in the absence of neural crest. We propose that through deposition of nidogen, and possibly other factors, neural crest cells contribute to a specific microenvironment which directs the proper movements of optic vesicle cells. In this model, the BM surrounding the RPE serves as a handbrake, restricting cell movements within the optic vesicle to ensure their correct speed and migratory course during optic cup morphogenesis. It will be interesting to investigate exactly what aspect of assembled BM function is required to support these specific morphogenetic events: future studies will address signaling, structural, and mechanical aspects of ECM assembly and activity.

Materials and methods

Zebrafish lines

Embryos from the following zebrafish (*Danio rerio*) mutant and transgenic lines were collected within 10 minutes of fertilization, raised at 28.5°C and staged according to hours post fertilization and morphology (Kimmel et al., 1995). Specifically, embryos were staged as 12 hpf by counting 6 somites, and at 24 hpf, pigment in the developing RPE becomes visible.

Mutant alleles:

tfap2a^{ts213}*;foxd3*^{zdf10} (Arduini et al., 2009). *nid1b*^{sa13713} contains a splice site mutation, and *nid2a*^{sa15802} contains a premature stop mutation (Kettleborough et al., 2013). The *alyron*^{z24} allele contains a C to A transversion in the coding sequence of the *paf1* gene, resulting in a premature stop mutation at tyrosine 281 (Y281*) (Mick Jurynec and David Grunwald, personal communication).

Transgenic alleles:

Tg(sox10:memRFP) ^{vu234} (Kirby et al., 2006), *Tg(sox10:GFP)*^{ba4} (Dutton et al., 2008), *Tg(bactin2:EGFP-CAAX)*^{z200} (Gordon et al., 2018), *Tg(hsp70:lyn-mCherry-2A-WT-Nid1a)*^{z202}*, Tg(hsp70:lyn-mCherry-2A-DI-Nid1a)*^{z203}.

Construction of Nid1a transgenic lines

Tg(hsp70:lyn-mCherry-2A-WT-Nid1a)^{z202}, a.k.a. *hs:WT-Nid1a* and *Tg(hsp70:lyn-mCherry-2A-DI-Nid1a)*^{z203}, a.k.a. *hs:DI-Nid1a* were generated using Gateway (Invitrogen, Carlsbad, CA) recombination. IMAGE Clone ID 8000296 (GE Dharmacon, Chicago, IL) was used as the template to PCR amplify cDNAs encoding wildtype and dominant-interfering Nid1a, these were ligated into pCS2FA prior to Gateway cloning. PCR primers were used to introduce the PTV-2A peptide (Provost et al., 2007) on the 5' end, and the SV40 late poly-adenylation signal on the 3' end of the zebrafish *nid1a* cDNA. Gateway 3' entry clones were generated via BP recombination and subsequently LR recombined into the pDEST-Tol2-CG2 destination vector which contains an *myl7:EGFP* expression cassette as a transgenesis marker (Kwan et al., 2007). 25 pg plasmid DNA was microinjected along with 50 pg mRNA encoding Tol2 transposase into single-cell wildtype embryos and screened for *myl7:EGFP* expression. Fluorescent embryos were raised to adulthood and outcrossed to generate stable transgenic lines.

Heat shocks

Embryos were transferred from a 28.5°C incubator and immediately overlaid with fresh, preheated 39°C E3. Embryos were incubated at 39°C for one hour on an Echotherm heating plate (Torrey Pines Scientific, Carlsbad, CA). Embryos were then transferred back to a 28.5°C incubator and grown to the indicated stage.

Allele identification/genotyping

All mutant alleles were PCR genotyped using either CAPS or dCAPS techniques (Neff et al., 1998). *tfap2a*^{ts213}: Forward (5'-

CGCTCAGGTCTTATAAATAGGCTACTAATAATGTTAC-3'), Reverse (5'-CTGAGAGGTGGCTATTTCCCGTTAAGATTCG-3'), mutant allele is cut with BlpI.

foxd3^{zdf10}: dCAPS Forward (5'-CGACTGCTTCGTCAAGATCCCACGGGAACCGGGCAACCCGGGCAAAGGCAACTACTGGACCCTCGACCCCCAGTCGGAAAATAT-3'), Reverse (5'-CAGGGGGAATGTACGGGTACTGC-3'), mutant allele is cut with SspI.

paf1^{z24}: Forward (5'-GTTCAGAGGTATGATGGATGAGG-3'), Reverse (5'-GTATGCAGCTTTATGAAAACACTC-3'), wildtype band is cut with NspI.

nid1b^{sa13713}*:* Forward (5'-ATCTGGGCAGTCCTGAAGGAATCGCC-3'), dCAPS Reverse (5'-GCACATTCTGGAGCTCATTCTGATTCTGATTTTAAACGTTCGCGCTGCTCTACTTTAGCGTGTTTTAGCCGTGTCATGCATTGGT-3'), wildtype allele is cut with KpnI.

nid2a^{15802}*:* Forward (5'-GACTTGCATTTCCAGTTACTCAGAATAAATATCTGTCTAGAC-3'), dCAPS Reverse (5'-CGGCCGTTGCCGTAAAAGCCGGAGTTGCAGTGACAGCAGAAGCCGGTGGAATGATCTGTACAGTGAGCGTTTAGACTGCAGT-3'), mutant allele is cut by ScaI.

RNA synthesis and injections

Capped mRNAs were synthesized using linearized pCS2 templates (pCS2-EGFP-CAAX, pCS2FA-H2A.F/Z-mCherry), the mMessage mMachine SP6 kit (AM1340, Invitrogen), purified using the Qiagen RNeasy Mini Kit (Qiagen, Hilden, Germany) and ethanol precipitated. 150-250 pg of each mRNA were microinjected into the cell of one-cell stage embryos. EGFP-CAAX mRNA was injected to visualize cell membranes, H2A.F/Z-mCherry mRNA was injected to visualize nuclei.

Antibody staining

Embryos for most antibodies were fixed at the indicated stage in 4% paraformaldehyde, permeabilized in PBST (PBS+0.5% Triton X-100), and blocked in PBST + 2% bovine serum albumin. Antibodies and concentrations are as follows: anti-Pax2a (GTX128127, Genetex, Irvine, CA), 1:200; anti-pSmad3 (ab52903, Abcam, Cambridge, MA), 1:200; anti-Laminin 1 (L9393, Sigma, St. Louis, MO), 1:100; anti-Fibronectin (F3648, Sigma), 1:100; anti-GFP (A10262, Invitrogen), 1:200.

After (Carrara et al., 2019), anti-Nidogen-1/Entactin (ab14511, Abcam) was used at 1:100 and required a modified embryo preparation after 4% paraformaldehyde fixation: embryos were permeabilized in 30 ug/mL Proteinase K for 15 minutes, and blocked in 0.8% PBST + 10% sheep serum + 1% bovine serum albumin. The antibody was applied in 0.8% PBST + 1% sheep serum + 1% bovine serum albumin.

Secondary antibodies used were Alexa Fluor 488 goat anti-mouse (A-11001, Invitrogen), Alexa Fluor 488 goat anti-rabbit (A-11008, Invitrogen), Alexa Fluor 488 goat anti-chicken (A-11039, Invitrogen) and incubated at 1:200. Nuclei were detected by incubation with 1 μM TO-PRO-3 iodide (T3605, Invitrogen). Embryos were cleared through a series of 30%/50%/70% glycerol (in PBS) prior to imaging.

In situ hybridization

Embryos were fixed at the indicated stage in 4% paraformaldehyde overnight at 4°C and dehydrated in 100% methanol. Color *in situ* hybridizations were performed similar to (Thisse and Thisse, 2008). Fluorescent *in situ* hybridizations were carried out as described previously (Lauter et al., 2014; Leerberg et al., 2017). Anti-GFP labeling and detection was performed after *in situ* hybridization and tyramide signal amplification.

In situ probes were synthesized from linearized pBluescript II SK+ templates (pBSII-Nid1a, pBSII-Nid1b, pBSII-Nid2a, pBSII-Nid2b) using T3 or T7 polymerases and DIG labeling mix (11277073910, Roche, Basel, Switzerland). All four probe sequences were synthesized (IDT gBlocks, IDT, San Jose, CA) and ligated into pBluescript II SK+.

Light Microscopy

For timelapse imaging, 12 hpf embryos were embedded in 1.6% low-melt agarose (in E3) in DeltaT dishes (Bioptechs, #0420041500 C), E3 was overlaid and the dish covered to prevent evaporation. For antibody stained or fluorescent *in situ* hybridization imaging, embryos were embedded in 1% low-melt agarose (in PBS) in Pelco glass-bottom dishes (#14027, Ted Pella, Redding, CA), PBS was overlaid to prevent evaporation.

Confocal images were acquired using a Zeiss LSM710 laser scanning confocal microscope. For timelapse imaging, datasets were acquired using the following parameters: 63 z-sections, 2.10 µm z-step, 40x water-immersion objective (1.2 NA). Time between z-stacks was 3 minutes 30 seconds (Movies 1, 2), 2 minutes 45 seconds (Movies 4, 6, 8, 10), and 2 minutes 30 seconds (Movies 5, 7, 9, 11). Movies 4-11 are average projections of EGFP-CAAX channel (grey) through ~60 µm centered at the dorsal/ventral midpoint of the optic vesicle with indicated nuclear trajectories overlaid. For all timelapse and antibody imaging, datasets were acquired without knowledge of embryo genotype. Embryos were de-embedded and genotyped after imaging was completed. Movies 5, 7, 9, 11 extend beyond 24 hpf, but all cell trajectory analyses were performed only up to the 24 hpf timepoint.

Brightfield images were acquired using an Olympus SZX16 stereomicroscope with either an Olympus DP26 or UC90 camera.

Transmission Electron Microscopy

24 hpf embryos were fixed, stained and embedded using the microwave-assisted tissue processing protocol described in (Czopka and Lyons, 2011). Tails were dissected from embryos prior to fixation and used for genotyping.

Our tissue sampling and analytical techniques have been described previously in detail (Anderson et al., 2011a, 2011b; Lauritzen et al., 2013; Marc et al., 2013, 2014).

The tissues were osmicated for 60 min in 0.5% OsO4 in 0.1 M cacodylate buffer, processed in maleate buffer for en bloc staining with uranyl acetate, and processed for resin embedding. The epoxy resin bloc with zebrafish tissue was sectioned in the horizontal plane at 70–90 nm onto polyvinyl formal resin coated copper slot grids for transmission electron microscopy (TEM) (Lauritzen et al., 2013; Marc and Jones, 2002).

Each TEM section was imaged on a JEOL JEM-1400 transmission electron microscope at 5000x or 20,000x and stored in 16- and 8-bit versions, as well as image pyramids of optimized tiles for web visualization with the Viking viewer (Anderson et al., 2011a, 2011b). Each image was captured as an array of image tiles at 330-465 tiles/slice (5000x) or 60-998 tiles/slice (20,000x) with 15% overlap.

Image processing and analysis

Images were processed using Fiji (Schindelin et al., 2012). Volume rendering was performed using FluoRender (Wan et al., 2009, 2017). For lateral view 3D rendering of the optic cup, the ectoderm was digitally erased in ImageJ prior to visualization in FluoRender. Invagination angles were measured as previously described (Bryan et al., 2016) and as diagrammed in Fig 1G, optic fissure angles were measured as previously described (Gordon et al., 2018) and diagrammed in Fig 1H. Pax2a and pSmad3-positive regions were measured as angles and diagrammed in Fig S2 L-M, by setting the vertex at the center of the lens

(Pax2a) or the innermost point of retinal invagination (pSmad3). The pSmad3^{+} portion of the lens was measured at the lens dorsal/ventral midpoint and calculated by dividing the area of pSmad3 staining by the total lens area. Lens roundness was measured by drawing a region of interest around the lens at its dorsal/ventral midpoint, followed by analysis using the Fiji Shape Descriptors measurement tool ("Roundness"). Nidogen coverage around the optic cup was measured at the dorsal/ventral midpoint of the optic cup by tracing the length of the nidogen-positive surface around each specific tissue of interest (brain, RPE or lens) and dividing that by the total length of that tissue. For the brain, this entailed measuring from the posterior limit of the image to the posterior margin of the olfactory placode; the entire RPE was measured starting where the temporal and nasal sides of that tissue contact the surface ectoderm; the entire circumference of the lens was measured. A segment was considered "nidogen-negative" if it was a clearly defined basal surface that lacked staining, adjacent to a nidogen-positive basal surface, and the signal-deficient region also lacked signal in neighboring sections in the z-stack. Laminin-1 and fibronectin coverage were measured in a similar fashion, but all optic tissues were binned into one surface around the optic cup. For all relevant measurements, the lens dorsal/ventral midpoint was derived independently for each optic cup from 3D image volume data, and validated via 3D rendering and visualization in FluoRender. Basement membrane lengths were measured using Viking: basal lamina coverage was considered continuous where both a discernable lamina lucida and lamina densa were visible lining the plasma membrane, otherwise that region was considered a discontinuous gap in coverage (Feitosa et al., 2011; Yurchenco and Schittny, 1990). Continuity percentages were calculated by dividing the length of continuous basement membrane visible along a tissue by the total length of the tissue surface. For Figure 5, *sox10:GFP*$^{+}$ cells were counted as near the optic fissure if they were located in the optic fissure or were in contact with a margin of the optic fissure. Individual cell tracking was

performed as described in (Kwan et al., 2012) using LongTracker; nuclei were visualized using H2A.F/Z-mCherry.

Statistical analysis

P-values for comparisons between two groups were calculated using a two-tailed Welch's T-test, Welch's t-test was chosen as it accounts for unequal sample sizes and inherently accounts for the possibility of unequal variance between groups. One-way ANOVA with a Tukey HSD post hoc test was used when comparing multiple groups. Statistical significance was assumed using a confidence interval of 95%. Box and whisker plots were generated using the ggplot2 package in RStudio. The upper and lower 'hinges' correspond to the first and third quartiles. The upper whisker extends from the upper hinge to the highest value within (1.5 * IQR), where IQR is the inter-quartile range. The lower whisker extends from the lower hinge to the lowest value within (1.5 * IQR). Data points outside of the ends of the whiskers (depicted as empty, white circles) are outliers.

Real-Time Quantitative PCR

Embryos were pooled at 24 hpf (n=30) and either flash-frozen in liquid nitrogen and stored at -80 ºC until use, or immediately homogenized using the QIAshredder (79654, Qiagen). Total RNA was then extracted using the RNeasy Mini Kit (74104, Qiagen) and stored at -80 ºC until use. cDNA was synthesized using the iScript cDNA Synthesis kit (1708890, BioRad, Hercules, CA) per the manufacturer's recommendations, such that 1 µg of RNA was loaded into each reaction. Three biological replicates were collected for each condition.

RT-qPCR primers were designed to span more terminal exon-exon junctions and produce amplicons of ~100 bp in length (Table 1). During optimization, products were both

gel analyzed and sequenced to ensure product specificity. All reactions utilized the PowerUp SYBR Green Master Mix (A25741, Applied BioSystems, Foster City, CA) and were performed on an Applied BioSystems 7900HT instrument. Efficiency (E) was calculated using a 4-point standard curve and optimized to be ~2.0 (Carleton, 2012). Wildtype 24 hpf cDNA was used to calculate efficiencies for *nid1a, nid1b,* and *nid2a*, while a 1:1 mixture of 24 hpf wildtype and MZ*nid1b*$^{-/-}$;MZ*nid2a*$^{-/-}$ cDNA was used to calculate the efficiency for *nid2b*. Cycling parameters were: 50 ºC (2 min) proceeded by 40 cycles of 95 ºC (2 min), 58 ºC (15 s), 72 ºC (1 min), then followed by a dissociation curve. Applied BioSystems software SDSv2.4 was used to determine cycle threshold (C_t) values and melting curves. All reactions were performed in triplicate with a no-template control.

RT-qPCR analysis was performed in Microsoft Excel using the ΔΔCt method (Livak and Schmittgen, 2001; Vandesompele et al., 2002). The relative quantity (RQ) of each *nid* gene was normalized to the reference gene *eef1a1l1* (Karra et al., 2015), and the normalized relative quantity (NRQ) was determined by normalizing 24 hpf *MZnid1b*$^{-/-}$*;MZnid2a*$^{-/-}$ expression to normalized 24 hpf wildtype expression (Figure 7I).

CRISPR-Cas9

Mutagenesis was achieved using the Alt-R CRISPR-Cas9 system developed by IDT (IDT, San Jose, CA). crRNAs were designed to target exon 3 of *nid1a* (5'-UCGCAACACAGAGGACACAGAGG-3') and exon 5 of *nid2b* (5'-GGACCUCCAUGGCUUUGCGGUGG-3'), or against a site within intron 5 of *slc24a5* (*golden*) (5'-AUAAAGUGAGGAGUGAUGGG-3'), published in (Hoshijima et al., 2016). The crRNA and tracrRNA were annealed into a dual guide (dg)RNA complex at a 1:1 ratio and stored at -20 ºC until use. On the day of injections, the ribonucleoprotein was assembled by incubating the dgRNA complexes (25 µM of total dgRNA) with the Cas9 Nuclease 3NLS

(25 µM) (1074181, IDT) at 37 ºC for 5 minutes (Kazuyuki Hoshijima and David Grunwald, personal communication). To visualize eye morphogenesis in crispants, as well as to determine which embryos had been successfully injected, 150 pg of capped EGFP-CAAX mRNA was co-injected with the ribonucleoprotein complex. Microinjections were performed into the cell of one-cell stage embryos.

Capillary Electrophoresis/Fragment Analysis

PCR primers were designed to generate a ~80 bp amplicon flanking the crRNA target site of either *nid1a* or *nid2b.* The 5' primer included a 5' 6-FAM fluorescent tag (IDT, San Jose, CA) to enable fragment detection. Genomic DNA was isolated from *MZnid1b*$^{-/-}$*;MZnid2a*$^{-/-}$ 1 dpf embryos injected with crRNA targeting the *nid1a* and *nid2b* loci or the *slc24a5* (*golden*) locus. Capillary electrophoresis was performed on an Applied BioSystems 3730 instrument.

Analysis was adapted from (Carrington et al., 2015). Fragments below 40 bp were removed from the analysis, as were fragments with a signal height below 1000. Six control, *golden*-injected embryos were analyzed for each mutagenesis experiment, and fragments above the specified thresholds were considered "WT" if detected in at least 2 control embryos. Fragments observed in *nid1a/nid2b*-injected embryos were identified as being "WT" if they were within ±0.5 bp length of fragments observed in control embryos, or were otherwise assigned as "Mutant" if they were of a length unobserved in control embryos. To determine the frequency of edited *nid1a* or *nid2b* alleles in the crRNA *nid1a/nid2b*-injected embryos, the height of either all "WT" peaks or all "Mutant" peaks was divided by total (WT + Mutant) peak height to yield a percent. Only crispants with a mutant allele frequency >70% for both *nid1a* and *nid2b* were used for further analysis.

Author Contributions

All authors performed experiments. C.D.B., M.A.C., and K.M.K. designed experiments, analyzed data, and wrote the manuscript.

Acknowledgments

We are grateful to Rodney Stewart, David Grunwald, and Mick Jurynec for reagents, and the University of Utah Centralized Zebrafish Animal Resource for zebrafish husbandry. Thanks to members of the Kwan lab for useful discussions and critical reading of the manuscript. This work was supported by grants from the National Eye Institute/National Institutes of Health (R01 EY025378, R01 EY025780 to K. M. K., R01 EY015128 to B. W. J., P30 EY014800 to the Moran Eye Center Vision Core). C. D. B. was supported by the University of Utah Developmental Biology Training Grant (National Institutes of Health T32HD007491). M. A. C. was supported by the University of Utah Genetics Training Grant (National Institutes of Health T32 GM007464).

Competing Interests

The authors declare no competing or financial interests.

References

Anderson, J.R., Jones, B.W., Watt, C.B., Shaw, M. V, Yang, J.H., Demill, D., Lauritzen, J.S., Lin, Y., Rapp, K.D., Mastronarde, D., et al. (2011a). Exploring the retinal connectome. Mol Vis *17*, 355–379.

Anderson, J.R., Mohammed, S., Grimm, B., Jones, B.W., Koshevoy, P., Tasdizen, T., Whitaker, R., and Marc, R.E. (2011b). The Viking viewer for connectomics: Scalable multi-user annotation and summarization of large volume data sets. J. Microsc. *241*, 13–28.

Arduini, B.L., Bosse, K.M., and Henion, P.D. (2009). Genetic ablation of neural crest cell diversification. Development *136*, 1987–1994.

Bader, B.L., Smyth, N., Nedbal, S., Baranowsky, A., Mokkapati, S., Miosge, N., Murshed, M., Nischt, R., Baranowsky, A., Mokkapati, S., et al. (2005). Compound Genetic Ablation of Nidogen 1 and 2 Causes Basement Membrane Defects and Perinatal Lethality in Mice. Mol. Cell. Biol. *25*, 6846–6856.

Bader, H.L., Lambert, E., Guiraud, A., Malbouyres, M., Driever, W., Koch, M., and Ruggiero, F. (2013). Zebrafish collagen XIV is transiently expressed in epithelia and is required for proper function of certain basement membranes. J. Biol. Chem. *288*, 6777–6787.

Bassett, E.A., Williams, T., Zacharias, A.L., Gage, P.J., Fuhrmann, S., and West-Mays, J.A. (2010). AP-2a knockout mice exhibit optic cup patterning defects and failure of optic stalk morphogenesis. Hum. Mol. Genet. *19*, 1791–1804.

Bohnsack, B.L., Kasprick, D.S., Kish, P.E., Goldman, D., and Kahana, A. (2012). A zebrafish model of Axenfeld-Rieger syndrome reveals that pitx2 regulation by Retinoic Acid is essential for ocular and craniofacial development. Investig. Ophthalmol. Vis. Sci. *53*, 7–22.

Böse, K., Nischt, R., Page, A., Bader, B.L., Paulsson, M., and Smyth, N. (2006). Loss of nidogen-1 and -2 results in syndactyly and changes in limb development. J. Biol. Chem. *281*, 39620–39629.

Bryan, C.D., Chien, C. Bin, and Kwan, K.M. (2016). Loss of laminin alpha 1 results in multiple structural defects and divergent effects on adhesion during vertebrate optic cup morphogenesis. Dev. Biol. *416*, 324–337.

Carleton, K.L. (2012). Quantification of Transcript Levels with Quantitative RT-PCR. In Molecular Methods for Evolutionary Genetics, pp. 279–295.

Carrara, N., Weaver, M., Piedade, W.P., Vöcking, O., and Famulski, J.K. (2019). Temporal characterization of optic fissure basement membrane composition suggests nidogen may be an initial target of remodeling. Dev. Biol.

Carrington, B., Varshney, G.K., Burgess, S.M., and Sood, R. (2015). CRISPR-STAT: An easy and reliable PCR-based method to evaluate target-specific sgRNA activity. Nucleic Acids Res. *43*, 1–8.

Chakraborty, S., Njah, K., Pobbati, A. V., Lim, Y.B., Raju, A., Lakshmanan, M., Tergaonkar, V., Lim, C.T., and Hong, W. (2017). Agrin as a Mechanotransduction Signal Regulating YAP through the Hippo Pathway. Cell Rep. *18*, 2464–2479.

Cretekos, C.J., and Grunwald, D.J. (1999). Alyron, an Insertional Mutation Affecting Early Neural Crest Development in Zebrafish. Dev. Biol. *210*, 322–338.

Czopka, T., and Lyons, D.A. (2011). Dissecting Mechanisms of Myelinated Axon Formation Using Zebrafish. In The Zebrafish: Disease Models and Chemical Screens, (Elsevier Inc.), pp. 25–62.

Dong, L.J., and Chung, A.E. (1991). The Expression of the Genes for Entactin, Laminin-a, Laminin-B1 and Laminin-B2 in Murine Lens Morphogenesis and Eye Development. Differentiation *48*, 157–172.

Dutton, J.R., Antonellis, A., Carney, T.J., Rodrigues, F.S., Pavan, W.J., Ward, A., and Kelsh, R.N. (2008). An evolutionarily conserved intronic region controls the spatiotemporal expression of the transcription factor Sox10. BMC Dev. Biol. *8*, 105.
Eberhart, J.K., He, X., Swartz, M.E., Yan, Y.L., Song, H., Boling, T.C., Kunerth, A.K., Walker, M.B., Kimmel, C.B., and Postlethwait, J.H. (2008). MicroRNA Mirn140 modulates Pdgf signaling during palatogenesis. Nat. Genet. *40*, 290–298.
Eiraku, M., Takata, N., Ishibashi, H., Kawada, M., Sakakura, E., Okuda, S., Sekiguchi, K., Adachi, T., and Sasai, Y. (2011). Self-organizing optic-cup morphogenesis in three-dimensional culture. Nature *472*, 51–56.
Ekblom, P., Ekblom, M., Fecker, L., Klein, G., Zhang, H.Y., Kadoya, Y., Chu, M.L., Mayer, U., and Timpl, R. (1994). Role of mesenchymal nidogen for epithelial morphogenesis in vitro. Development *120*, 2003–2014.
El-Brolosy, M., Rossi, A., Kontarakis, Z., Kuenne, C., Guenther, S., Fukuda, N., Takacs, C., Lai, S.-L., Fukuda, R., Gerri, C., et al. (2019). Genetic compensation triggered by mutant mRNA degradation. Nature *568*, 193–197.
Feitosa, N.M., Richardson, R., Bloch, W., and Hammerschmidt, M. (2011). Basement Membrane Diseases in Zebrafish.
Fox, J.W., Mayer, U., Nischt, R., Aumailley, M., Reinhardt, D., Wiedemann, H., Mann, K., Timpl, R., Krieg, T., and Engel, J. (1991). Recombinant nidogen consists of three globular domains and mediates binding of laminin to collagen type IV. EMBO J. *10*, 3137–3146.
Fuhrmann, S., Levine, E.M., and Reh, T.A. (2000). Extraocular mesenchyme patterns the optic vesicle during early eye development in the embryonic chick. Development *127*, 4599–4609.
Gage, P.J., Rhoades, W., Prucka, S.K., and Hjalt, T. (2005). Fate maps of neural crest and mesoderm in the mammalian eye. Investig. Ophthalmol. Vis. Sci. *46*, 4200–4208.
Gestri, G., Osborne, R.J., Wyatt, A.W., Gerrelli, D., Gribble, S., Stewart, H., Fryer, A., Bunyan, D.J., Prescott, K., Collin, J.R.O., et al. (2009). Reduced TFAP2A function causes variable optic fissure closure and retinal defects and sensitizes eye development to mutations in other morphogenetic regulators. Hum. Genet. *126*, 791–803.
Gestri, G., Bazin-Lopez, N., Scholes, C., and Wilson, S.W. (2018). Cell Behaviors during Closure of the Choroid Fissure in the Developing Eye. Front. Cell. Neurosci. *12*, 1–12.
Gordon, H.B., Lusk, S., Carney, K.R., Wirick, E.O., Murray, B.F., and Kwan, K.M. (2018). Hedgehog signaling regulates cell motility and optic fissure and stalk formation during vertebrate eye morphogenesis. Development *145*, dev165068.
Grocott, T., Johnson, S., Bailey, A.P., and Streit, A. (2011). Neural crest cells organize the eye via TGF-β and canonical Wnt signalling. Nat. Commun. *2*, 266–269.
Hayes, J.M., Hartsock, A., Clark, B.S., Napier, H.R.L., Link, B.A., and Gross, J.M. (2012). Integrin 5/Fibronectin1 and focal adhesion kinase are required for lens fiber morphogenesis in zebrafish. Mol. Biol. Cell *23*, 4725–4738.
Heermann, S., Schütz, L., Lemke, S., Krieglstein, K., and Wittbrodt, J. (2015). Eye morphogenesis driven by epithelial flow into the optic cup facilitated by modulation of bone morphogenetic protein. Elife *4*, 1–17.
Hendrix, R.W., and Zwaan, J. (1975). The matrix of the optic vesicle-presumptive lens interface during induction of the lens in the chicken embryo. J. Embryol. Exp. Morphol. *33*, 1023–1049.
Hero, I. (1990). Optic fissure closure in the normal cinnamon mouse: An ultrastructural study. Investig. Ophthalmol. Vis. Sci. *31*, 197–216.
Hero, I., Farjah, M., and Scholtz, C.L. (1991). The prenatal development of the optic fissure in colobomatous microphthalmia. Investig. Ophthalmol. Vis. Sci. *32*, 2622–2635.

Hilfer, S.R. (1983). Development of the eye of the chick embryo. Scan. Electron Microsc. 1353–1369.
Ho, M.S.P., Böse, K., Mokkapati, S., Nischt, R., and Smyth, N. (2008). Nidogens — Extracellular Matrix Linker Molecules. Microsc. Res. Tech. *395*, 387–395.
Hoshijima, K., Jurynec, M.J., and Grunwald, D.J. (2016). Precise Editing of the Zebrafish Genome Made Simple and Efficient. Dev. Cell *36*, 654–667.
Huang, J., Rajagopal, R., Liu, Y., Dattilo, L.K., Shaham, O., Ashery-Padan, R., and Beebe, D.C. (2011). The mechanism of lens placode formation: A case of matrix-mediated morphogenesis. Dev. Biol. *355*, 32–42.
Ivanovitch, K., Cavodeassi, F., and Wilson, S.W. (2013). Precocious acquisition of neuroepithelial character in the eye field underlies the onset of eye morphogenesis. Dev. Cell *27*, 293–305.
James, A., Lee, C., Williams, A.M., Angileri, K., Lathrop, K.L., and Gross, J.M. (2016). The hyaloid vasculature facilitates basement membrane breakdown during choroid fissure closure in the zebrafish eye. Dev. Biol. *419*, 262–272.
Johnston, M.C., Noden, D.M., Hazelton, R.D., Coulombre, J.L., and Coulombre, A.J. (1979). Origins of avian ocular and periocular tissues. Exp. Eye Res. *29*, 27–43.
Kadoya, Y., Salmivirta, K., Talts, J.F., Kadoya, K., Mayer, U., Timpl, R., and Ekblom, P. (1997). Importance of nidogen binding to laminin γ1 for branching epithelial morphogenesis of the submandibular gland. Development *124*, 683–691.
Kalluri, R. (2003). Basement membranes: Structure, assembly and role in tumour angiogenesis. Nat. Rev. Cancer *3*, 422–433.
Karra, R., Knecht, A.K., Kikuchi, K., and Poss, K.D. (2015). Myocardial NF-κB activation is essential for zebrafish heart regeneration. Proc. Natl. Acad. Sci. *112*, 13255–13260.
Kettleborough, R.N.W., Busch-Nentwich, E.M., Harvey, S.A., Dooley, C.M., De Bruijn, E., Van Eeden, F., Sealy, I., White, R.J., Herd, C., Nijman, I.J., et al. (2013). A systematic genome-wide analysis of zebrafish protein-coding gene function. Nature *496*, 494–497.
Kimmel, C.B., Ballard, W.W., Kimmel, S.R., Ullmann, B., and Schilling, T.F. (1995). Stages of embryonic development of the zebrafish. Dev. Dyn. *203*, 253–310.
Kirby, B.B., Takada, N., Latimer, A.J., Shin, J., Carney, T.J., Kelsh, R.N., and Appel, B. (2006). In vivo time-lapse imaging shows dynamic oligodendrocyte progenitor behavior during zebrafish development. Nat. Neurosci. *9*, 1506–1511.
Kudoh, T., Tsang, M., Hukriede, N.A., Chen, X., Dedekian, M., Clarke, C.J., Kiang, A., Schultz, S., Epstein, J.A., Toyama, R., et al. (2001). A gene expression screen in zebrafish embryogenesis. Genome Res. *11*, 1979–1987.
Kwan, K.M. (2014). Coming into focus: The role of extracellular matrix in vertebrate optic cup morphogenesis. Dev. Dyn. *243*, 1242–1248.
Kwan, K.M., Fujimoto, E., Grabher, C., Mangum, B.D., Hardy, M.E., Campbell, D.S., Parant, J.M., Yost, H.J., Kanki, J.P., and Chien, C. Bin (2007). The Tol2kit: A multisite gateway-based construction Kit for Tol2 transposon transgenesis constructs. Dev. Dyn. *236*, 3088–3099.
Kwan, K.M., Otsuna, H., Kidokoro, H., Carney, K.R., Saijoh, Y., and Chien, C.-B. (2012). A complex choreography of cell movements shapes the vertebrate eye. Development *139*, 359–372.
Langenberg, T., Kahana, A., Wszalek, J.A., and Halloran, M.C. (2008). The eye organizes neural crest cell migration. Dev. Dyn. *237*, 1645–1652.
Lauritzen, J.S., Anderson, J.R., Jones, B.W., Watt, C.B., Mohammed, S., Hoang, J. V., and Marc, R.E. (2013). ON Cone Bipolar Cell Axonal Synapses in the OFF Inner Plexiform Layer of the Rabbit Retina. J. Comp. Neurol. *521*, 977–1000.

Lauter, G., Söll, I., and Hauptmann, G. (2014). Sensitive Whole-Mount Fluorescent In Situ Hybridization in Zebrafish Using Enhanced Tyramide Signal Amplification. Methods Mol. Biol. *1082*, 175–185.
Lee, J., Willer, J.R., Willer, G.B., Smith, K., Gregg, R.G., and Gross, J.M. (2008). Zebrafish blowout provides genetic evidence for Patched1-mediated negative regulation of Hedgehog signaling within the proximal optic vesicle of the vertebrate eye. Dev. Biol. *319*, 10–22.
Leerberg, D.M., Sano, K., and Draper, B.W. (2017). Fibroblast growth factor signaling is required for early somatic gonad development in zebrafish. PLOS Genet. 1–28.
Li, W., and Cornell, R.A. (2007). Redundant activities of Tfap2a and Tfap2c are required for neural crest induction and development of other non-neural ectoderm derivatives in zebrafish embryos. Dev. Biol. *304*, 338–354.
Li, Z., Joseph, N.M., and Easter, S.S. (2000). The morphogenesis of the zebrafish eye, including a fate map of the optic vesicle. Dev. Dyn. *218*, 175–188.
Livak, K.J., and Schmittgen, T.D. (2001). Analysis of relative gene expression data using real-time quantitative PCR and the 2-ΔΔCT method. Methods *25*, 402–408.
Lössl, P., Kölbel, K., Tänzler, D., Nannemann, D., Ihling, C.H., Keller, M. V., Schneider, M., Zaucke, F., Meiler, J., and Sinz, A. (2014). Analysis of nidogen-1/laminin γ1 interaction by cross-linking, mass spectrometry, and computational modeling reveals multiple binding modes. PLoS One *9*.
Lupo, G., Gestri, G., O'Brien, M., Denton, R.M., Chandraratna, R.A.S., Ley, S. V, Harris, W.A., and Wilson, S.W. (2011). Retinoic acid receptor signaling regulates choroid fissure closure through independent mechanisms in the ventral optic cup and periocular mesenchyme. Proc. Natl. Acad. Sci. U. S. A. *108*, 8698–8703.
Marc, R.E., and Jones, B.W. (2002). Molecular phenotyping of retinal ganglion cells. J. Neurosci. *22*, 413–427.
Marc, R.E., Jones, B.W., Watt, C.B., Anderson, J.R., Sigulinsky, C., and Lauritzen, S. (2013). Retinal connectomics: Towards complete, accurate networks. Prog. Retin. Eye Res. *37*, 141–162.
Marc, R.E., Anderson, J.R., Jones, B.W., Sigulinsky, C.L., and Lauritzen, J.S. (2014). The AII amacrine cell connectome: a dense network hub. Front. Neural Circuits *8*, 1–13.
Martinez-Morales, J.R., Rembold, M., Greger, K., Simpson, J.C., Brown, K.E., Quiring, R., Pepperkok, R., Martin-Bermudo, M.D., Himmelbauer, H., and Wittbrodt, J. (2009). Ojoplano-mediated basal constriction is essential for optic cup morphogenesis. Development *136*, 2165–2175.
Miesfeld, J.B., Gestri, G., Clark, B.S., Flinn, M.A., Poole, R.J., Bader, J.R., Besharse, J.C., Wilson, S.W., and Link, B.A. (2015). Yap and Taz regulate retinal pigment epithelial cell fate. Development *142*, 3021–3032.
Neff, M.M., Neff, J.D., Chory, J., and Pepper, A.E. (1998). dCAPS, a simple technique for the genetic analysis of single nucleotide polymorphisms: experimental applications in Arabidopsis thaliana genetics. Plant J. *14*, 387–392.
Nelson, D.A., and Larsen, M. (2015). Heterotypic control of basement membrane dynamics during branching morphogenesis. Dev. Biol. *401*, 103–109.
Nguyen, C.T., Langenbacher, A., Hsieh, M., and Chen, J.N.O. (2010). The PAF1 complex component Leo1 is essential for cardiac and neural crest development in zebrafish. Dev. Biol. *341*, 167–175.
Nicolás-Pérez, M., Kuchling, F., Letelier, J., Polvillo, R., Wittbrodt, J., and Martínez-Morales, J.R. (2016). Analysis of cellular behavior and cytoskeletal dynamics reveal a constriction mechanism driving optic cup morphogenesis. Elife *5*, 1–24.

Peterson, P.E., Pow, C.S., Wilson, D.B., and Hendrickx, A.G. (1995). Localisation of glycoproteins and glycosaminoglycans during early eye development in the macaque. J. Anat. *186 (Pt 1*, 31–42.
Picker, A., Cavodeassi, F., Machate, A., Bernauer, S., Hans, S., Abe, G., Kawakami, K., Wilson, S.W., and Brand, M. (2009). Dynamic coupling of pattern formation and morphogenesis in the developing vertebrate retina. PLoS Biol. *7*.
Pozzi, A., Yurchenco, P.D., and Iozzo, R. V. (2017). The nature and biology of basement membranes. Matrix Biol. *57–58*, 1–11.
Provost, E., Rhee, J., and Leach, S.D. (2007). Viral 2A peptides allow expression of multiple proteins from a single ORF in transgenic zebrafish embryos. Genesis *45*, 625–629.
Pujuguet, P., Simian, M., Liaw, J., Timpl, R., Werb, Z., and Bissell, M.J. (2000). Nidogen-1 regulates laminin-1-dependent mammary-specific gene expression. J. Cell Sci. *113*, 849–858.
Reinhardt, D., Mann, K., Nischt, R., Fox, J.W., Chu, M.L., Krieg, T., and Timpl, R. (1993). Mapping of nidogen binding sites for collagen type IV, heparan sulfate proteoglycan, and zinc. J. Biol. Chem. *268*, 10881–10887.
Salmivirta, K., Talts, J.F., Olsson, M., Sasaki, T., Timpl, R., and Ekblom, P. (2002). Binding of mouse nidogen-2 to basement membrane components and cells and its expression in embryonic and adult tissues suggest complementary functions of the two nidogens. Exp. Cell Res.
Schindelin, J., Arganda-Carreras, I., Frise, E., Kaynig, V., Longair, M., Pietzsch, T., Preibisch, S., Rueden, C., Saalfeld, S., Schmid, B., et al. (2012). Fiji: an open-source platform for biological-image analysis. Nat. Methods *9*, 676–682.
Schmitt, E.A., and Dowling, J.E. (1994). Early eye morphogenesis in the zebrafish, Brachydanio rerio. J. Comp. Neurol. *344*, 532–542.
Schook, P. (1980). Morphogenetic movements during the early development of the chick eye. A light microscopic and spatial reconstructive study. Acta Morphol. Neerl. Scand. *18*, 1–30.
Sedykh, I., Yoon, B., Roberson, L., Moskvin, O., Dewey, C.N., and Grinblat, Y. (2017). Zebrafish zic2 controls formation of periocular neural crest and choroid fissure morphogenesis. Dev. Biol. *429*, 92–104.
Senior, R.M., Griffin, G.L., Mudd, M.S., Moxley, M.A., Longmore, W.J., and Pierce, R.A. (1996). Entactin expression by rat lung and rat alveolar epithelial cells. Am. J. Respir. Cell Mol. Biol. *14*, 239–247.
Sidhaye, J., and Norden, C. (2017). Concerted action of neuroepithelial basal shrinkage and active epithelial migration ensures efficient optic cup morphogenesis. Elife *6*, 1–29.
Svoboda, K.K., and O'Shea, K.S. (1987). An analysis of cell shape and the neuroepithelial basal lamina during optic vesicle formation in the mouse embryo. Development *100*, 185–200.
Thesleff, I. (2003). Epithelial-mesenchymal signalling regulating tooth morphogenesis. J. Cell Sci. *116*, 1647–1648.
Thisse, B., and Thisse, C. (2004). Fast Release Clones: A High Throughput Expression Analysis. ZFIN Direct Data Submiss.
Thisse, C., and Thisse, B. (2008). High-resolution in situ hybridization to whole-mount zebrafish embryos. Nat. Protoc. *3*, 59–69.
Tuckett, F., and Morriss-Kay, G.M. (1986). The distribution of fibronectin, laminin and entactin in the neurulating rat embryo studied by indirect immunofluorescence. J. Embryol. Exp. Morphol. *94*, 95–112.
Vandesompele, J., De Preter, K., Pattyn, F., Poppe, B., Van Roy, N., De Paepe, A., and Speleman, F. (2002). Accurate normalization of real-time quantitative RT-PCR data by geometric averaging of multiple internal control genes. Genome Biol. *34*, research0034.1.

Walls, G.L. (1942). The vertebrate eye and its adaptive radiation (Hafner Publishing Company).
Wan, Y., Otsuna, H., Chien, C. Bin, and Hansen, C. (2009). An interactive visualization tool for multi-channel confocal microscopy data in neurobiology research. IEEE Trans. Vis. Comput. Graph. *15*, 1489–1496.
Wan, Y., Otsuna, H., Holman, H.A., Bagley, B., Ito, M., Lewis, A.K., Colasanto, M., Kardon, G., Ito, K., and Hansen, C. (2017). FluoRender: Joint freehand segmentation and visualization for many-channel fluorescence data analysis. BMC Bioinformatics *18*, 1–15.
Wang, W.-D., Melville, D.B., Montero-Balaguer, M., Hatzopoulos, A.K., and Knapik, E.W. (2011). Tfap2a and Foxd3 regulate early steps in the development of the neural crest progenitor population. Dev. Biol. *360*, 173–185.
Weiss, O., Kaufman, R., Michaeli, N., and Inbal, A. (2012). Abnormal vasculature interferes with optic fissure closure in lmo2 mutant zebrafish embryos. Dev. Biol. *369*, 191–198.
Wells, K.L., Gaete, M., Matalova, E., Deutsch, D., Rice, D., and Tucker, A.S. (2013). Dynamic relationship of the epithelium and mesenchyme during salivary gland initiation: the role of Fgf10. Biol. Open *2*, 981–989.
Willem, M., Miosge, N., Halfter, W., Smyth, N., Jannetti, I., Burghart, E., Timpl, R., and Mayer, U. (2002). Specific ablation of the nidogen-binding site in the laminin γ1 chain interferes with kidney and lung development. Development *129*, 2711–2722.
Williams, A.L., and Bohnsack, B.L. (2015). Neural crest derivatives in ocular development: Discerning the eye of the storm. Birth Defects Res. Part C - Embryo Today Rev. *105*, 87–95.
Yurchenco, P.D., and Schittny, J.C. (1990). Molecular architecture of basement membranes. FASEB J. *4*, 1577–1590.
Zhu, P., Ma, Z., Guo, L., Zhang, W., Zhang, Q., Zhao, T., Jiang, K., Peng, J., and Chen, J. (2017). Short body length phenotype is compensated by the upregulation of nidogen family members in a deleterious nid1a mutation of zebrafish. J. Genet. Genomics *44*, 553–556.

Figures

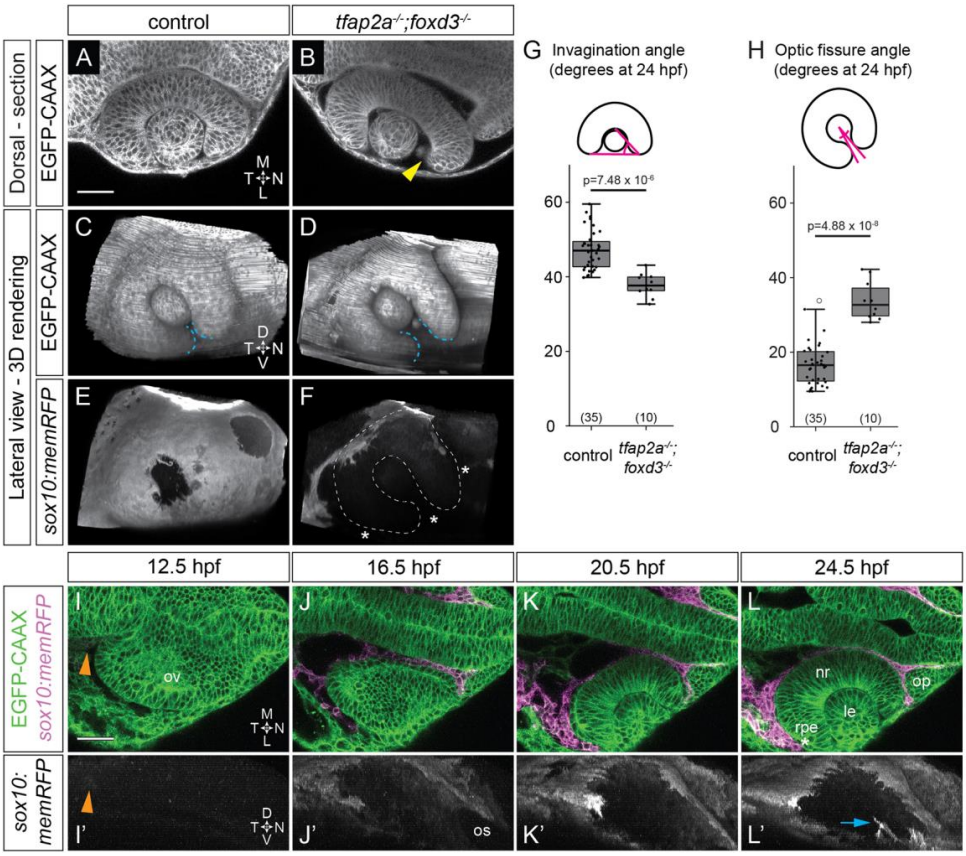

Figure 1. Optic cup morphogenesis requires neural crest
(A-F) Dorsal (A-B) and lateral (C-F) views of 24 hpf *Tg(bactin2:EGFP-CAAX);Tg(sox10:memRFP)* double transgenic control and *tfap2a;foxd3* mutant optic cups. Single confocal sections (A-B) at the d/v midpoint of the lens. Arrowhead (B) marks gap where nasal retina fails to fully enwrap lens. White dashed lines (F), optic cup boundaries. Blue dashed lines (C-D), optic fissure margins. Asterisks (F), regions lacking neural crest. (G-H) Quantification of invagination angle (G) and optic fissure angle (H) measured as shown in inset diagrams. n (embryos) shown at base of graphs, from 3 experiments. P-values were calculated using one-way ANOVA with Tukey HSD post hoc test.
(I-L) Timelapse imaging (12.5-24.5 hpf) of *Tg(bactin2:EGFP-CAAX);Tg(sox10:memRFP)* double transgenic embryo. Dorsal view, single confocal sections (I-L) and lateral view, 3D rendering of magenta channel from same dataset (I'-L'). Arrowheads (I, I') indicate RFP^{+} neural crest. Asterisk (L) marks RPE between neural crest and neural retina. Arrow (L') marks neural crest-derived cells entering the optic fissure.
Scale bars, 50 μm. ov, optic vesicle; os, optic stalk; nr, neural retina; rpe, retinal pigment epithelium; le, lens; op, olfactory placode. M, medial; L, lateral; D, dorsal; V, ventral; N, nasal; T, temporal.

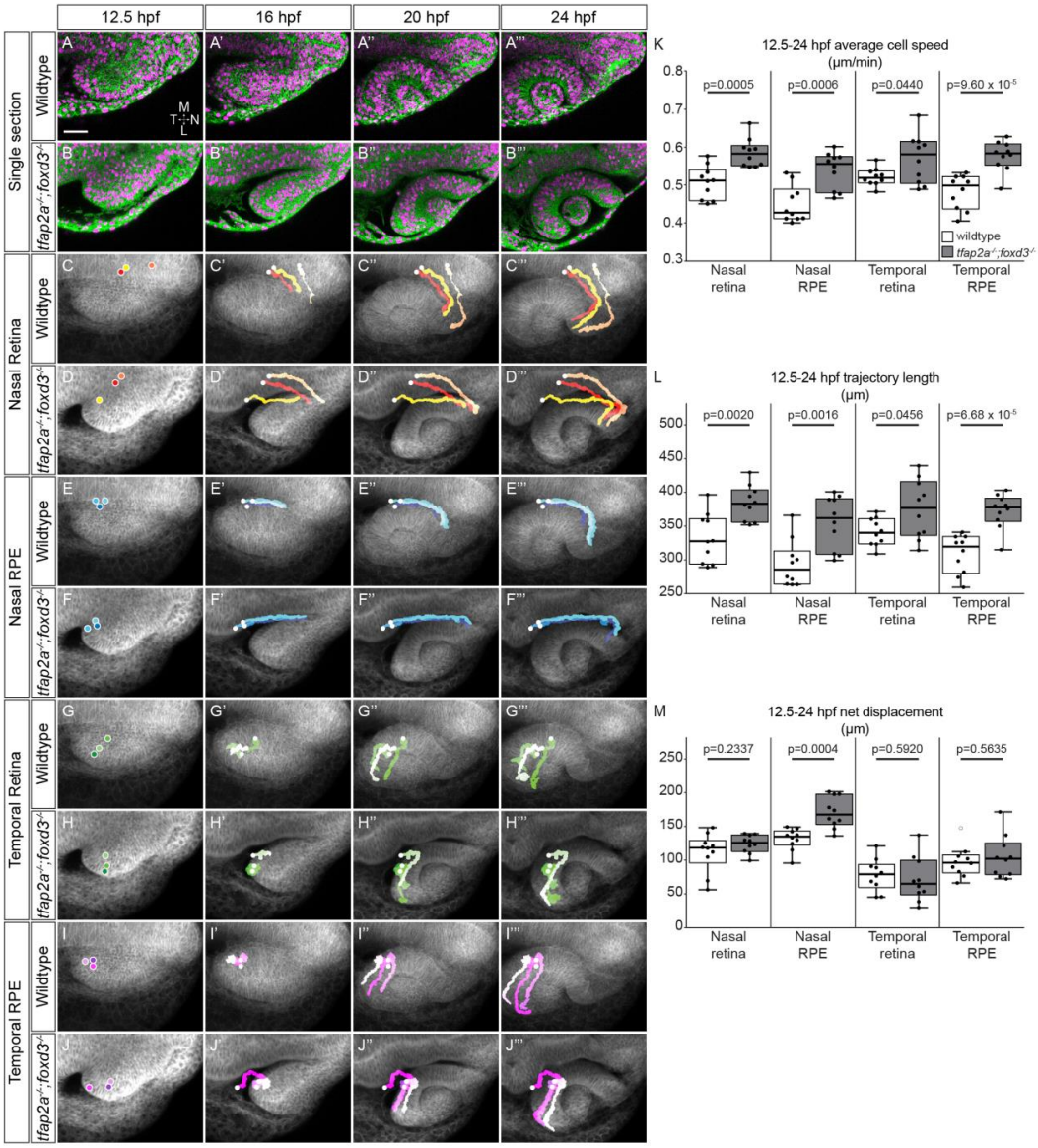

Figure 2. Optic cup cell movements are disrupted in *tfap2a;foxd3* mutants
(A-J) Timelapse imaging (12.5-24 hpf) of optic cup morphogenesis of wildtype and *tfap2a;foxd3* mutant embryos. (A-B) Dorsal view, single confocal sections from wildtype (A) and *tfap2a;foxd3* mutant (B) 4D datasets. EGFP-CAAX (green) labels cell membranes; H2A.F/Z-mCherry (magenta) labels nuclei.
(C-J) Average projections of EGFP-CAAX channel (grey) with indicated nuclear trajectories overlaid. Trajectories generated by accumulating nuclear selections over time.
(K-M) Average 3D cell speed (K), total 3D trajectory length (L), and 3D net displacement (M) of cells contributing to each region at 24 hpf. n=10 cells from each region (2 embryos/genotype, 5 cells each). P-values were calculated using Welch's t-test.
Scale bar, 50 µm. M, medial; L, lateral; N, nasal; T, temporal.

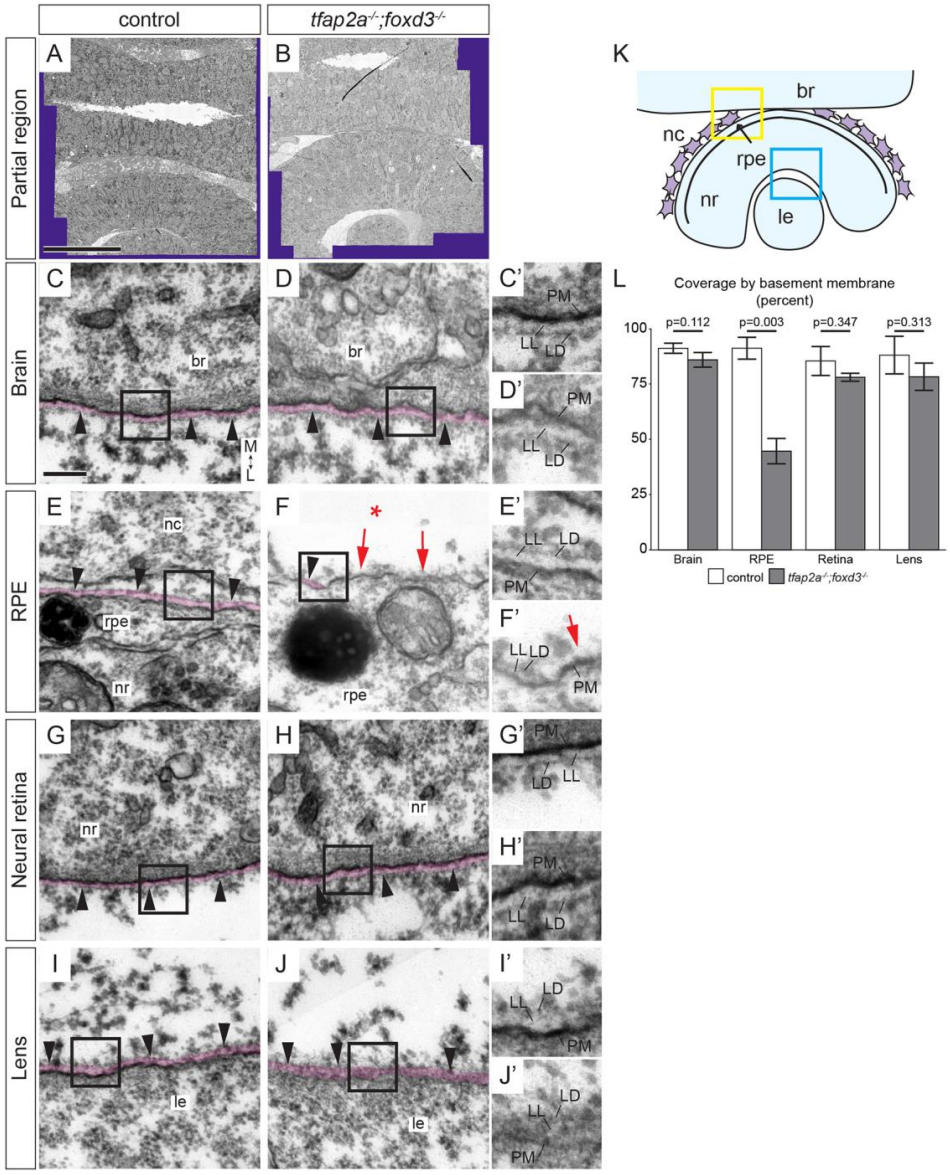

Figure 3. The basement membrane around the RPE is disrupted in *tfap2a;foxd3* mutants

(A-B) Tiled arrays of 2 nm/pixel resolution transmission electron micrographs of eyes and forebrains of 24 hpf wildtype control (A) and *tfap2a;foxd3* mutant (B) zebrafish. Acquired regions extend across the brain and through the opposite eye. Purple area is the boundary of captured images.

(C-J) Basement membranes around the brain, RPE, neural retina, and lens in control (C, E, G, I) and *tfap2a;foxd3* mutant (D, F, H, J) embryos imaged at high resolution (~0.5 nm/pixel). Basement membranes pseudocolored magenta, and black boxes are enlarged in C'-J' to aid visualization. The basement membrane around the RPE of *tfap2a;foxd3* mutant embryos appears discontinuous (F, F' *red arrows*) compared to wildtype (E, E'); other basement

membranes appear normal and continuous (*black arrowheads*). Labels in (C'-J'), PM, plasma membrane; LL, lamina lucida; LD, lamina densa.
(K) Diagram of tissues imaged. Boxes indicate brain/neural crest/RPE (yellow) and neural retina/lens (blue) regions reimaged at high resolution (~0.5 nm/pixel).
(L) Quantification of percent of tissue surface lined with discernable, continuous basement membrane containing both lamina lucida and lamina densa. P-values were calculated using Welch's t-test, error bars=±2xSEM.
Scale bars, 50 μm (A), 200 nm (C). Magnification (C-J)=10,000x, (C'-J')=20,000x. br, brain; nc, neural crest; nr, neural retina; rpe, retinal pigment epithelium; le, lens. All images transverse sections, anterior views. M, medial; L, lateral.

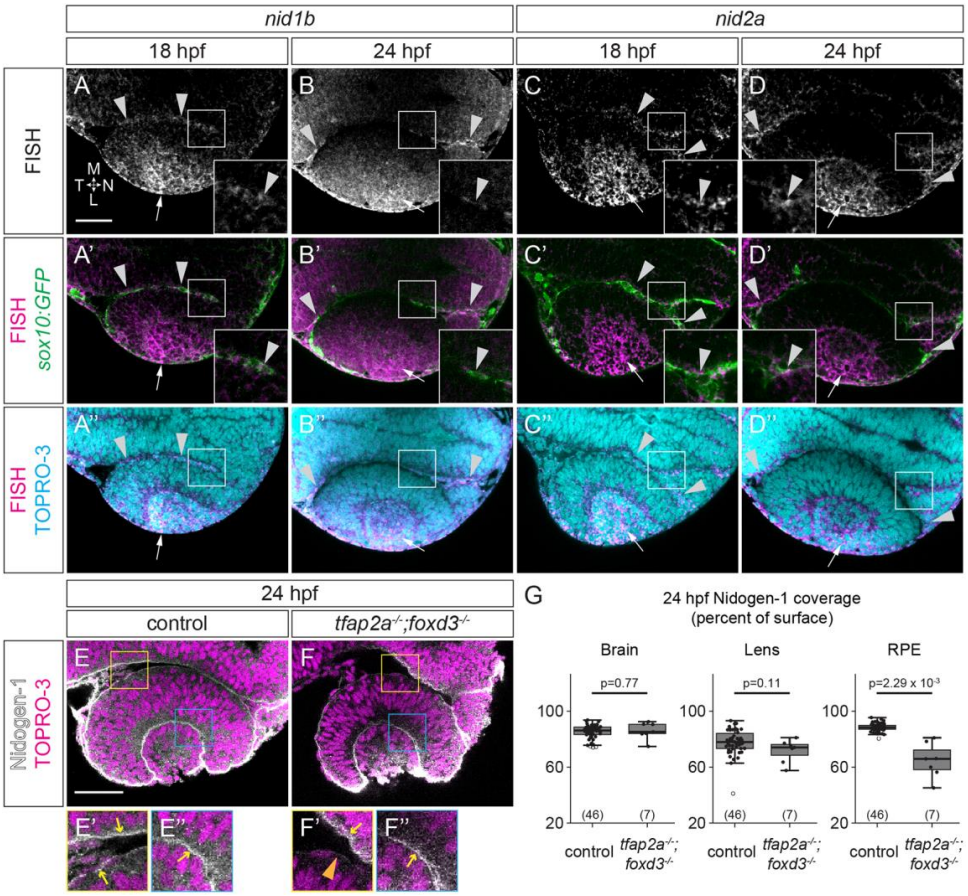

Figure 4. Nidogen mRNA and protein are expressed around the developing eye
(A-D) Fluorescence *in situ* hybridization (FISH) for *nid1b* (A, B) and *nid2a* (C, D) in *Tg(sox10:GFP)* embryos. FISH (*magenta*) merged with *sox10:GFP* expression (*green*, A'-D') to visualize colocalization between FISH and GFP^{+} neural crest (*arrowheads*). FISH merged with nuclei (TO-PRO-3, *cyan*, A"-D"). Arrows mark lens expression.
(E-F) Immunofluorescence for nidogen-1. In 24 hpf control embryos, nidogen-1 protein (*grayscale*) is detected along the brain and RPE (yellow box in E, arrows in E') and lens-retina interface (blue box in E, arrow in E"). In 24 hpf *tfap2a;foxd3* mutants, nidogen-1 is discontinuous around the RPE (F', *orange arrowhead*), but still lines the brain (F', *arrow*) and lens-retina interface (F", *arrow*).
(G) Measurements of nidogen-1 protein coverage around the brain, lens, and RPE. Percentages were calculated by dividing the length of antibody labeling over the total tissue surface length. P-values calculated using Welch's t-test. n (embryos) shown at base of graphs. Scale bar, 50 μm. Dorsal view, single confocal sections. M, medial; L, lateral; N, nasal; T, temporal.

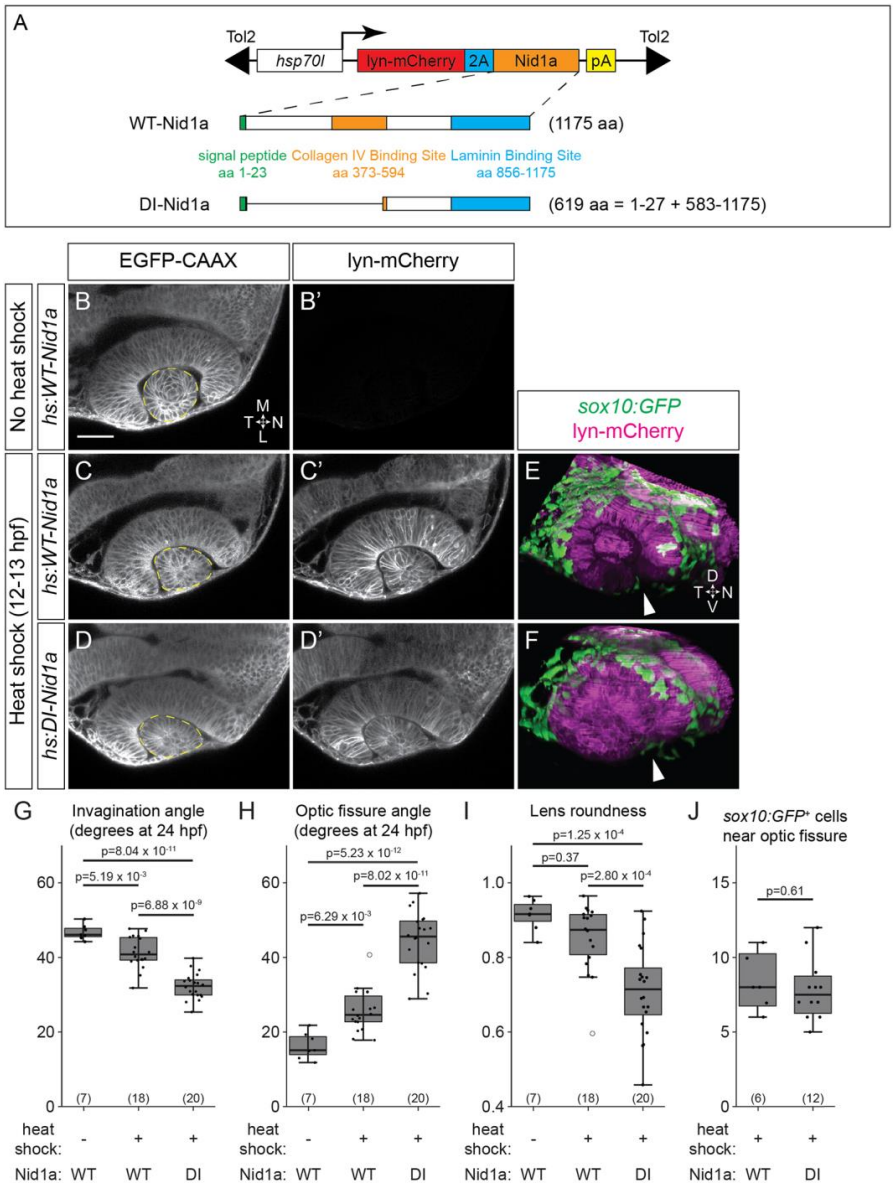

Figure 5. Dominant-interfering nidogen disrupts optic cup morphogenesis
(A) Schematics of full length (WT) and dominant-interfering (DI) zebrafish nidogen-1a and transgene constructs.
(B-D) *Tg(bactin2:EGFP-CAAX)* transgenics also carrying either *hs:WT-Nid1a* (B-C) or *hs:DI-Nid1a* (D) transgenes. Control embryos (B), not heat shocked, are lyn-mCherry^{-} (B'); experimental embryos were heat shocked 12-13 hpf (C-D). Dorsal view, single confocal sections.
(E-F) *Tg(sox10:GFP)*$^{+}$*;hs:WT-Nid1a* (E) or *hs:DI-Nid1a* (F) transgenics heat shocked 12-13 hpf. GFP^{+} neural crest cells migrate around the optic cup and into the optic fissure (arrowheads) in both conditions. Lateral view, 3D renderings, 24 hpf.

(G-J) Quantification of invagination angle (G), optic fissure angle (H), lens roundness (I), and *sox10:GFP*$^{+}$ cell number at the optic fissure (J). Dashed lines (B-D) mark lens outlines used for roundness measurements. *sox10:GFP*$^{+}$ cells were counted as near the optic fissure if they were located in the optic fissure or were in contact with a margin of the optic fissure. n (embryos) shown at base of graphs, from 1-3 experiments. P values were calculated using one-way ANOVA with Tukey HSD post hoc test (G-I) or Welch's t-test (J).
Scale bar, 50 μm. M, medial; L, lateral; D, dorsal; V, ventral; N, nasal; T, temporal.

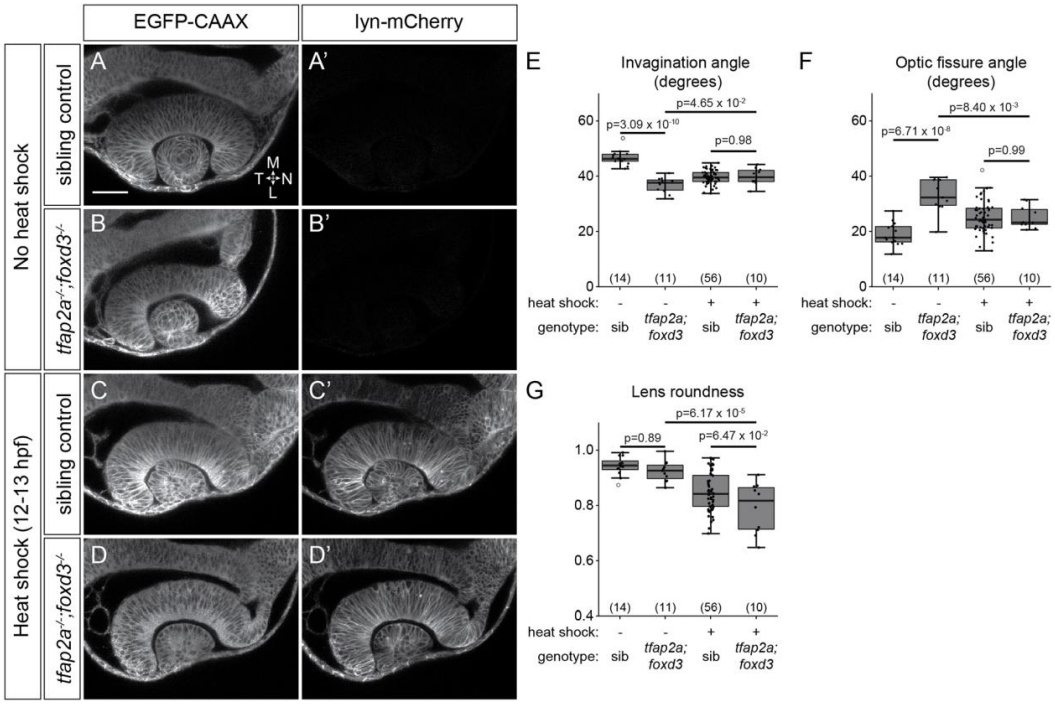

Figure 6. Nid1a overexpression partially rescues optic cup morphogenesis in *tfap2a;foxd3* mutants

(A-D) Double transgenic embryos (*Tg(bactin2:EGFP-CAAX);Tg(hs:WT-Nid1a)*): sibling control and *tfap2a;foxd3* mutant embryos not heat shocked (A-B), or heat shocked 12-13 hpf (C-D). Dorsal view, single confocal sections, 24 hpf.

(E-G) Quantification of invagination angle (E), optic fissure angle (F), and lens roundness (G). n (embryos) shown in the base of the graph, from 2-3 experiments. P values were calculated using one-way ANOVA with Tukey HSD post hoc test.

Scale bar, 50 μm. M, medial; L, lateral; N, nasal; T, temporal.

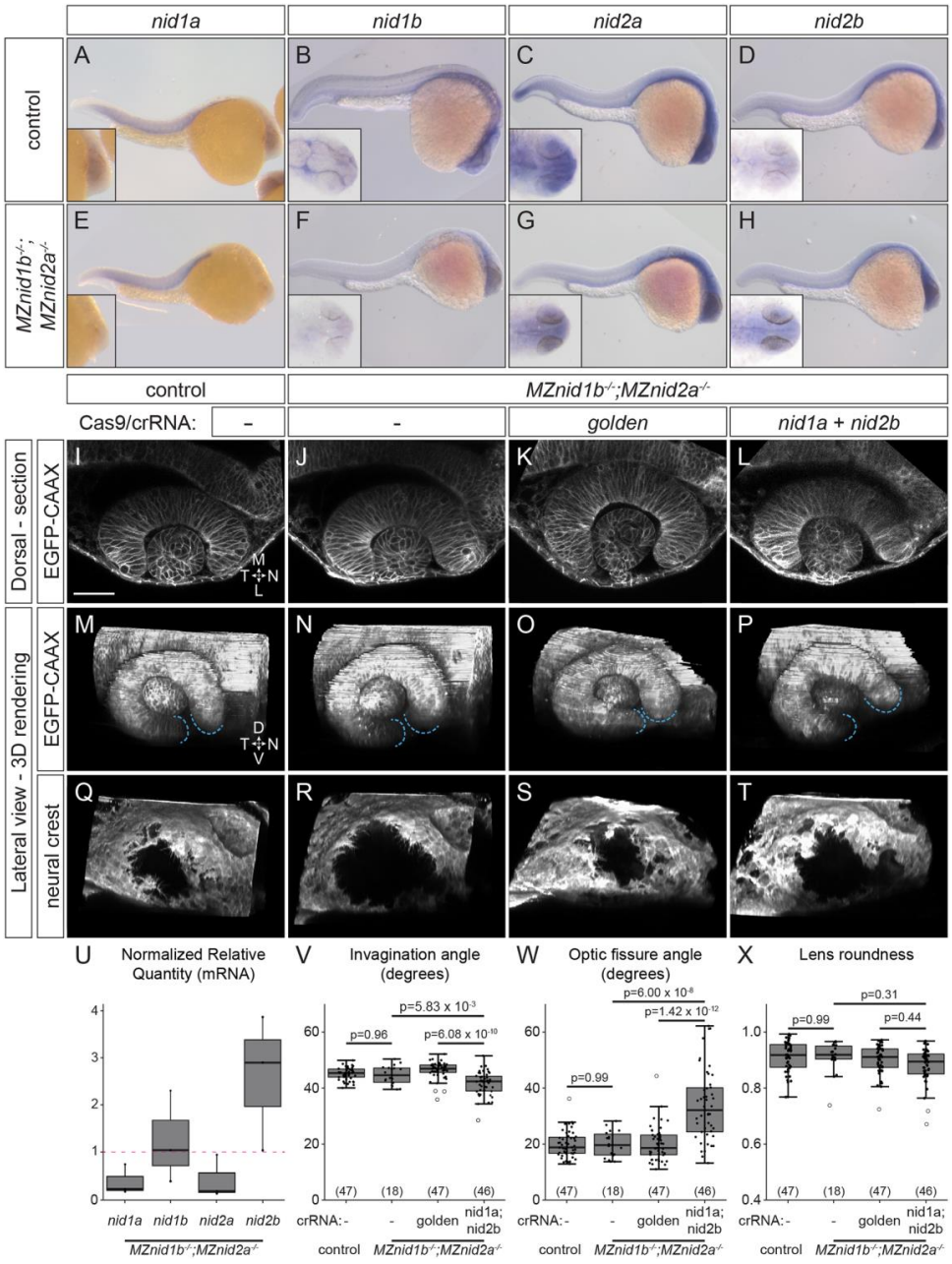

Figure 7. Nidogen is required for optic cup morphogenesis
(A-H) Whole mount *in situ* hybridization for *nidogens* in 24 hpf control (A-D) and *MZnid1b;MZnid2a* mutant (E-H) embryos. Insets show zoomed view of head.
(I-T) Optic cup morphology and neural crest localization in EGFP-CAAX mRNA injected, *Tg(sox10:memRFP)*$^{+}$ embryos: control (I, M, Q), *MZnid1b;MZnid2a* mutant (J, N, R), *golden* crispant *MZnid1b;MZnid2a* mutant (K, O, S), and *nid1a;nid2b* crispant *MZnid1b;MZnid2a* mutant (L, P, T).

(U) RT-qPCR quantification of nidogen transcripts in *MZnid1b;MZnid2a* mutant embryos, normalized to wildtype control expression levels (magenta dashed line, NRQ=1). Results from 3 biological replicates run in triplicate.
(V-X) Quantification of invagination angle (V), optic fissure angle (W), and lens roundness (X). n (embryos) shown in base of graph. P values were calculated using one-way ANOVA with Tukey HSD post hoc test.
Scale bar, 50 μm. M, medial; L, lateral; D, dorsal; V, ventral; N, nasal; T, temporal.

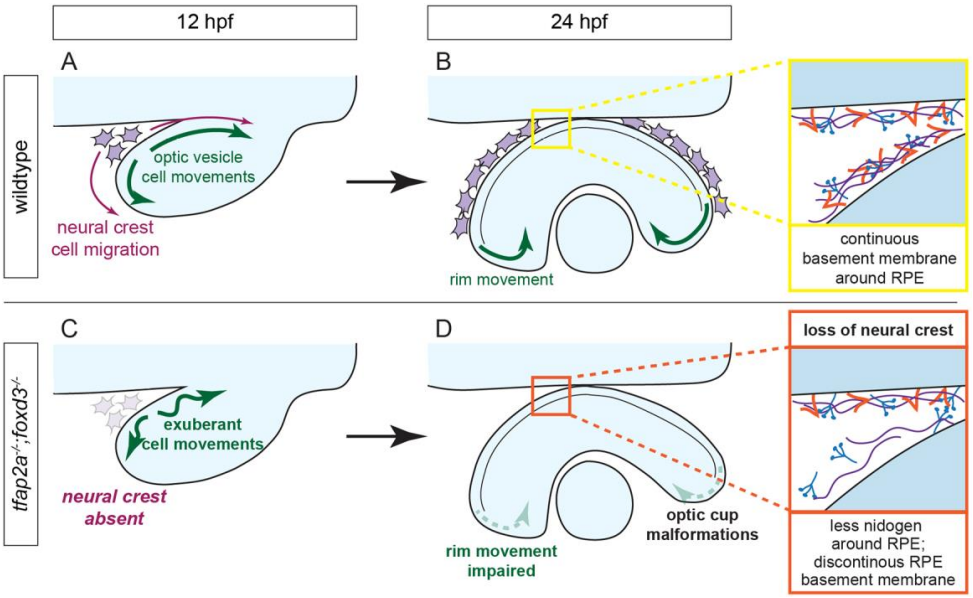

Figure 8. Model of optic cup morphogenesis in wildtype and *tfap2a;foxd3* double mutant zebrafish

(A-B) Optic cup morphogenesis in a wildtype embryo. Neural crest cells migrate around the optic vesicle and enable efficient movement of optic vesicle cells (A). Cells undergo rim movement and contribute to the neural retina, partially enabled by the presence of a continuous basement membrane along the surface of the RPE (B).

(C-D) Optic cup morphogenesis in a *tfap2a;foxd3* double mutant embryo. Most neural crest cells are absent, resulting in optic vesicle cells that move faster and farther than in wildtype embryos (C). Rim movement is impaired in the absence of a complete, continuous basement membrane around the RPE, resulting in optic cup malformations (D).

Tables

Table 1. RT-qPCR Primers

Gene	5' (5' – 3')	3' (5' – 3')
nid1a	CATGAAAATGCTGTCTGTTTCAA	GCAACGCGTCTTTTCACGTTCTG
nid1b	CAGCCGGACTTCCACAAC	CGCTGAACTGCTGTCTGATGG
nid2a	GCCCCCATCGGAGGTCTATTTG	CCGAGTGAATTCAGCACCGGTG
nid2b	GCCTTACAGGACTCGGTTG	CGTCCAAAATCTGTCCAATACA
eef1a1l1	CCTCTTTCTGTTACCTGGCAAA	CTTTTCCTTTCCCATGATTGA

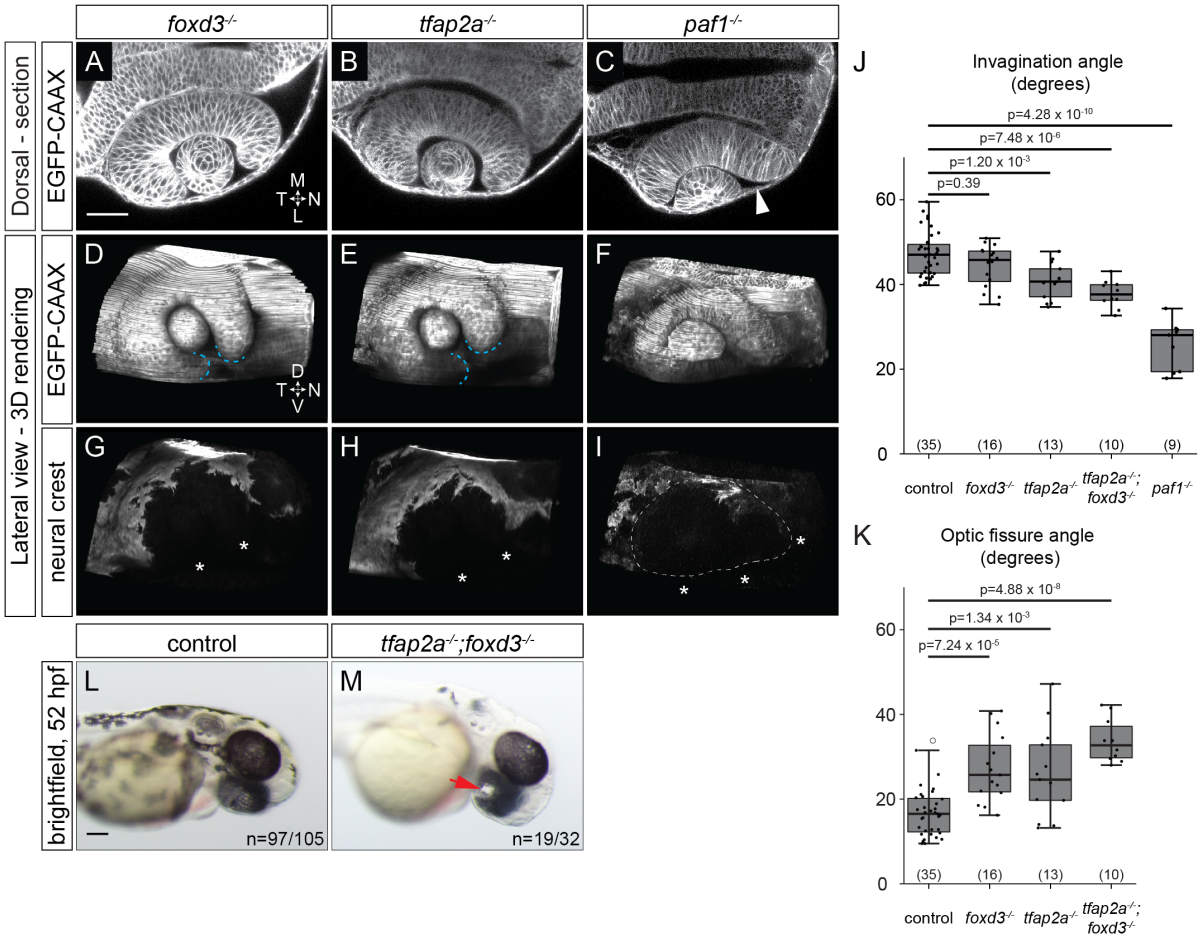

Figure S1. Related to Figure 1. Optic cup morphogenesis defects in neural crest mutants
(A-I) 24 hpf optic cups of *Tg(bactin2:EGFP-CAAX);Tg(sox10:memRFP)* double transgenic *foxd3* (A, D, G), *tfap2a* (B, E, H), and *paf1* (C, F, I) mutant embryos. Single sections shown are at the dorsal/ventral midpoint of the lens; lateral views are a 3D rendering of the corresponding 4D dataset.
(J-K) Quantification of invagination angles (J) and optic fissure angles (K) measured as in Figure 1. Results are from 2-3 experiments; n (embryos) shown at base of each graph. P-values calculated using Welch's t-test, white circles are outliers.
(L-M) Brightfield images of 52 hpf control and *tfap2a;foxd3* mutant embryos. Red arrow in (P) indicates coloboma.
Scale bars: 50 µm (A), 100 µm (L). M, medial; L, lateral; D, dorsal; V, ventral; N, nasal; T, temporal.

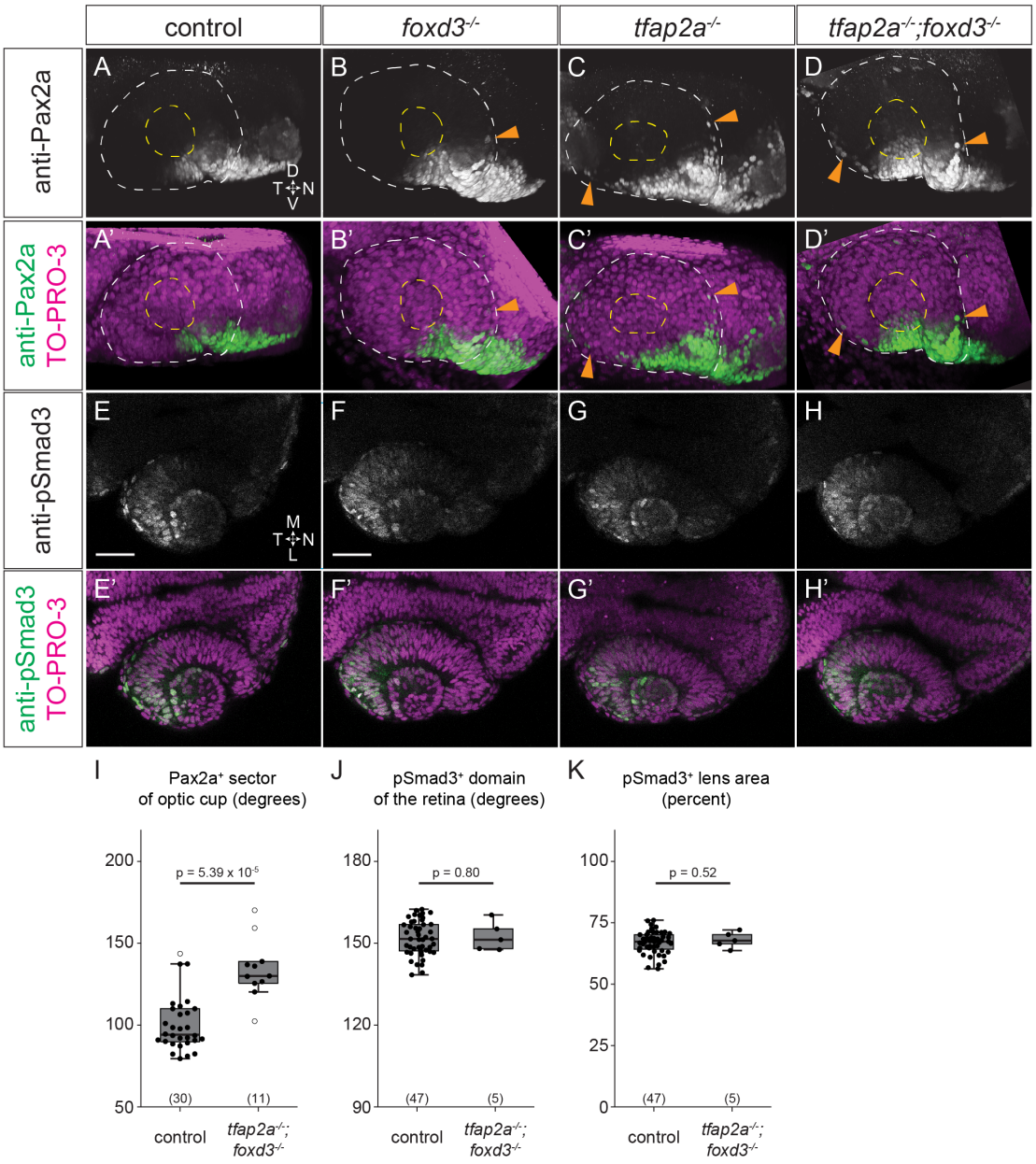

Figure S2. Related to Figure 1. Pax2a is expanded in neural crest mutants while TGF-beta signaling is unaffected

(A-D) Immunofluorescence of Pax2a. Lateral view, 3D renderings of 24 hpf control (A), *foxd3* mutant (B), *tfap2a* mutant (C) and *tfap2a;foxd3* double mutant (D) eyes. White dashed circles denote the boundary of the optic cup, yellow dashed circles display the boundary of the lens. Orange arrowheads in (B-D) indicate RPE cells which ectopically express Pax2a. Immunofluorescence merged with nuclei counterstained with TO-PRO-3 (magenta, A'-D').

(E-H) Immunofluorescence of phospho-Smad3. Dorsal view, single confocal sections of 24 hpf control (E), *foxd3* mutant (F), *tfap2a* mutant (G) and *tfap2a;foxd3* double mutant (H) eyes. Immunofluorescence merged with nuclei counterstained with TO-PRO-3 (magenta, E'-H'). Sections shown are at the dorsal/ventral lens midpoint.

(I-M) Measurements of the Pax2a expressing portion of control and *tfap2a;foxd3* mutant eyes. $Pax2a^{+}$ sectors of the eye were measured from the lateral surface as diagrammed in (L), with the vertex of the angle set at the center of the lens. $pSmad3^{+}$ retinal domain was measured from the lateral margin of the optic cup as diagrammed in (M), with the vertex of the angle set at the innermost point of the central retina. $pSmad3^{+}$ lens area was calculated by dividing the area of the lens expressing pSmad3 over the total lens area. P-values calculated using Welch's t-test, white circles are outliers. Results are from 2-3 experiments; n (embryos) shown in the base of the graph.

Scale bar, 50 μm. M, medial; L, lateral; D, dorsal; V, ventral; N, nasal; T, temporal.

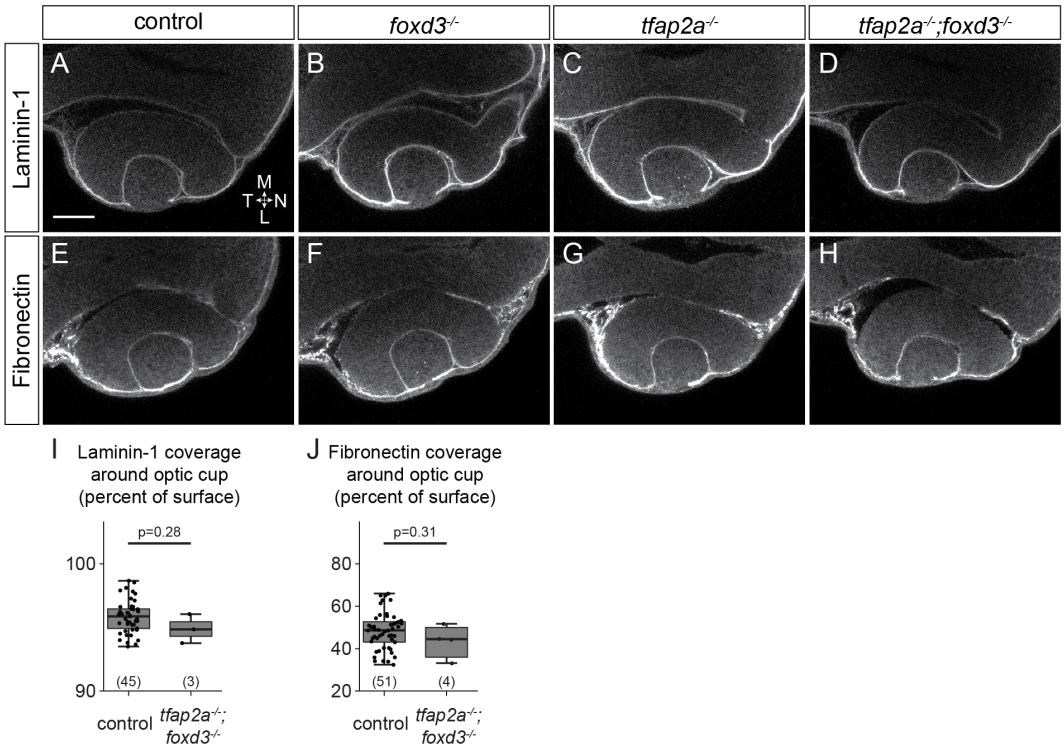

Figure S3. Related to Figure 3. Laminin and fibronectin localization are unaffected in *tfap2a;foxd3* mutants

(A-H) Immunofluorescence for laminin-1 and fibronectin. At 24 hpf, both laminin (A-D) and fibronectin (E-H) are found around the developing optic cup in all genotypes shown.

(I-J) Measurements of laminin-1 (I) and fibronectin (J) distribution around the optic cup. Percentages were calculated by dividing the length of antibody labeling over the total optic cup surface length. P-values calculated using Welch's t-test, results are from 2 experiments each. Scale bar, 50 μm. Dorsal view, single confocal sections. M, medial; L, lateral; N, nasal; T, temporal.

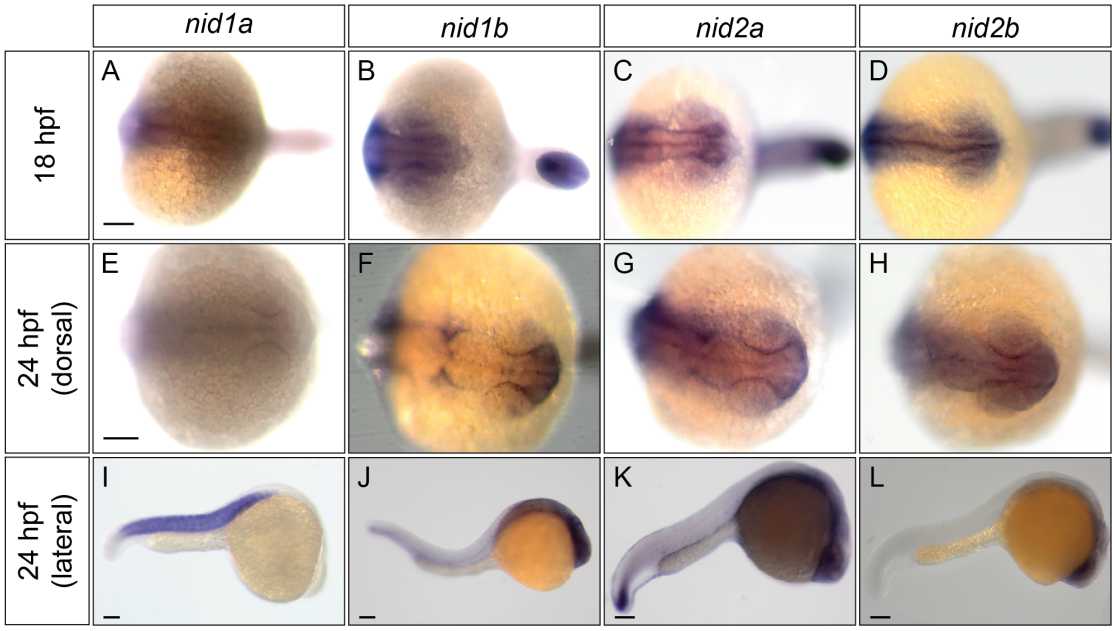

Figure S4. Related to Figure 4. Zebrafish nidogen mRNA expression patterns at 18 and 24 hpf

(A-L) Whole mount *in situ* hybridization with anti-sense probes against indicated *nidogen* mRNA at 18 hpf (A-D) or 24 hpf (E-L). Scale bars, 100 μm.

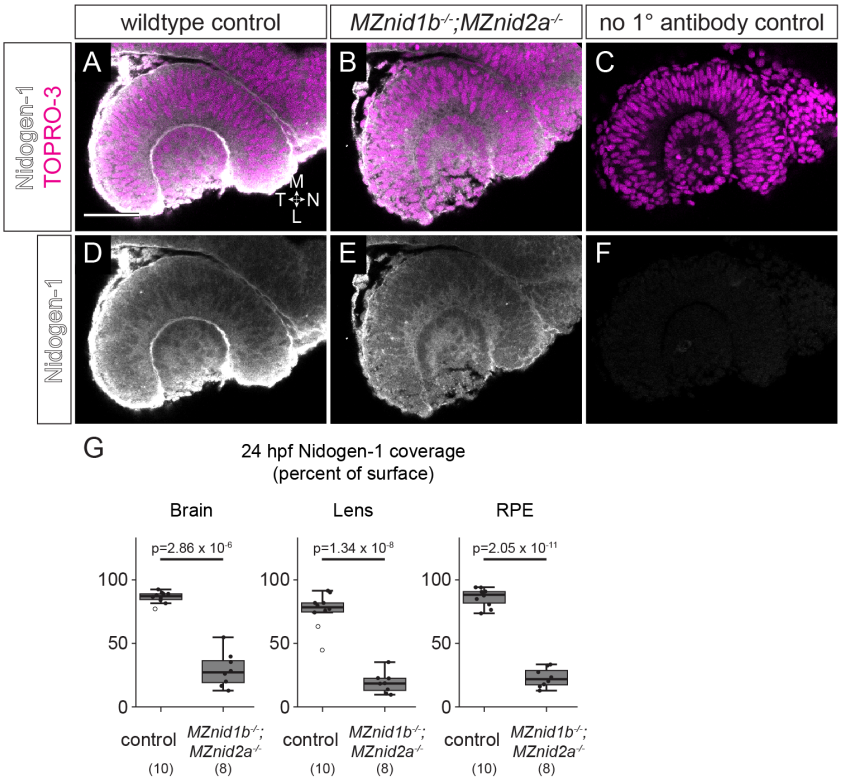

Figure S5. Related to Figure 7. Nidogen-1 protein is reduced in maternal-zygotic *nid1b;nid2a* double mutants

(A-F) Immunofluorescence for nidogen-1. At 24 hpf, nidogen is present in basement membranes throughout the head of wildtype control embryos (A, D), but is severely reduced in the basement membranes of *MZnid1b;MZnid2a* double mutants (B, E). A wildtype embryo which was not exposed to primary antibody is shown as a control in (C, F).

(G) Measurements of nidogen-1 protein coverage around the brain, lens, and RPE. Percentages were calculated by dividing the length of antibody labeling over the total tissue surface length. P-values calculated using Welch's t-test. n (embryos) shown below the corresponding genotype. Scale bar, 50 μm. Dorsal view, single confocal sections. M, medial; L, lateral; N, nasal; T, temporal.

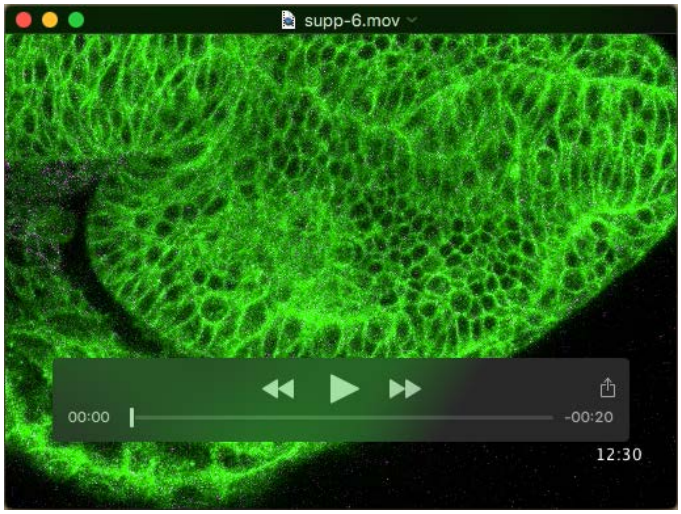

Movie 1. Related to Figure 1. Neural crest migration during optic cup morphogenesis. 12.5-24.5 hpf timelapse of a *Tg(β-actin2:EGFP-CAAX);Tg(sox10:memRFP)* double transgenic embryo. EGFP-CAAX labels all cell membranes (green), while membrane-bound RFP (magenta) labels only the neural crest. Dorsal view, single confocal section through the dorsal/ventral midpoint of the optic cup. Nasal (anterior) is to the right, temporal (posterior) to the left. ΔT between z-stacks, 3 minutes 30 seconds.

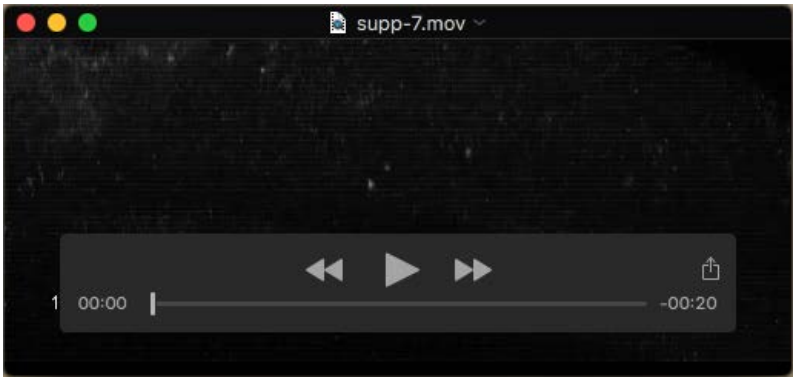

Movie 2. Related to Figure 1. Neural crest migration during optic cup morphogenesis. 12.5-24.5 hpf timelapse of a *Tg(β-actin2:EGFP-CAAX);Tg(sox10:memRFP)* double transgenic embryo. Lateral view, 3D rendering of the same timelapse dataset shown in Movie 1. Only the RFP channel is shown (grayscale) to enable visualization of neural crest cell migration. Nasal (anterior) is to the right, temporal (posterior) to the left, dorsal to the top, ventral to the bottom. ΔT between z-stacks, 3 minutes 30 seconds

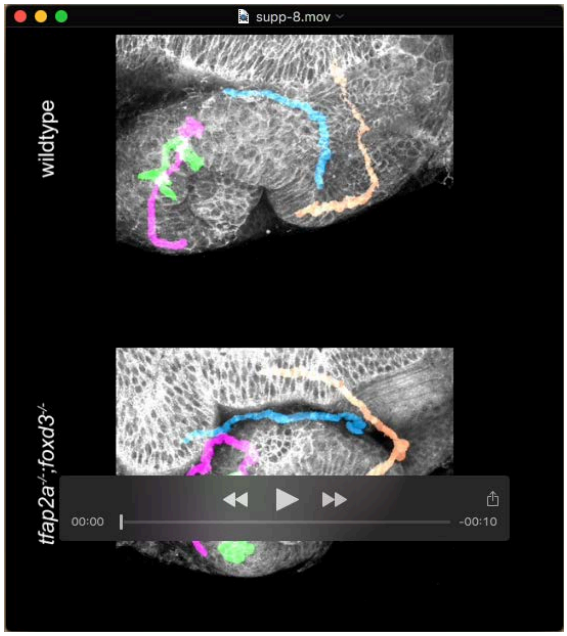

Movie 3. Related to Figure 2. Nuclear trajectories visualized in in three dimensions. 3D rendered rotation of 24 hpf timepoints showing representative 4-dimensional trajectories of nuclei from cells in the nasal retina (orange), nasal RPE (blue), temporal retina (green), and temporal RPE (magenta). Membrane channel is displayed in grayscale.

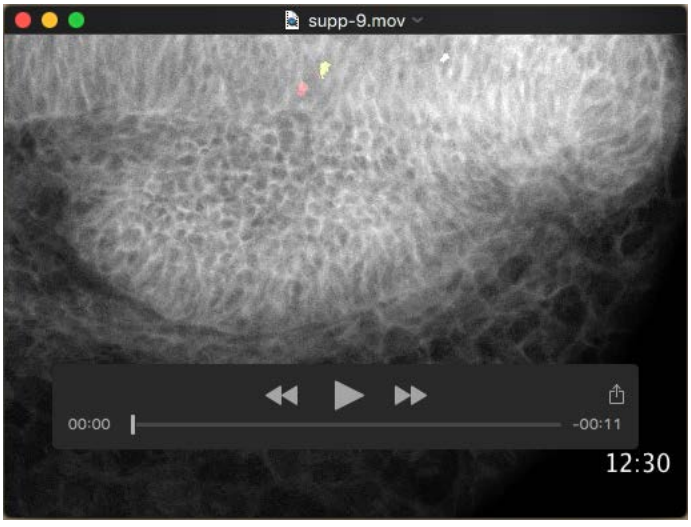

Movie 4. Related to Figure 2. Wildtype nasal retina nuclear trajectories from 12.5-24 hpf. Representative trajectories over membrane channel average (grayscale). ΔT between z-stacks, 2 minutes 45 seconds.

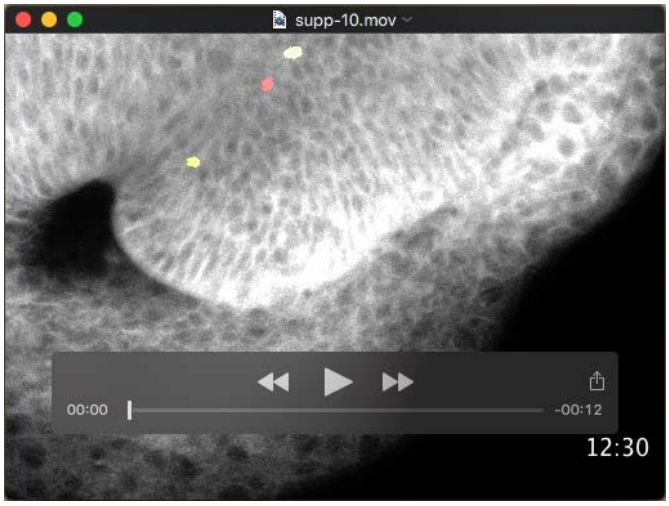

Movie 5. Related to Figure 2. *tfap2a;foxd3* double mutant nasal retina nuclear trajectories from 12.5-24 hpf. Representative trajectories over membrane channel average (grayscale). ΔT between z-stacks, 2 minutes 30 seconds.

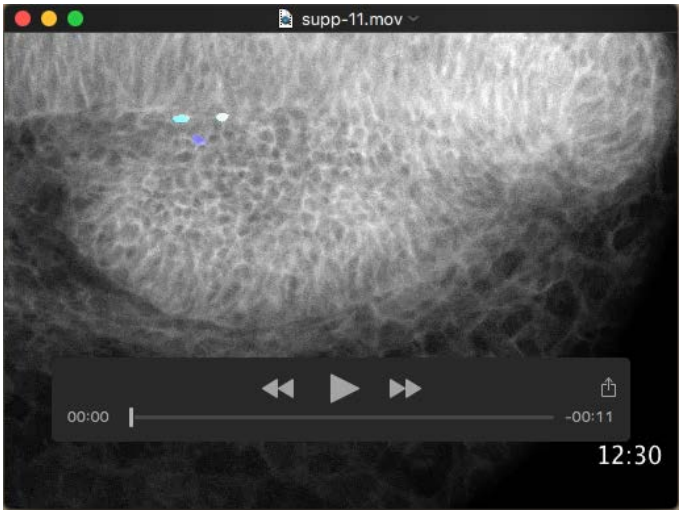

Movie 6. Related to Figure 2. Wildtype nasal RPE nuclear trajectories from 12.5-24 hpf. Representative trajectories over membrane channel average (grayscale). ΔT between z-stacks, 2 minutes 45 seconds.

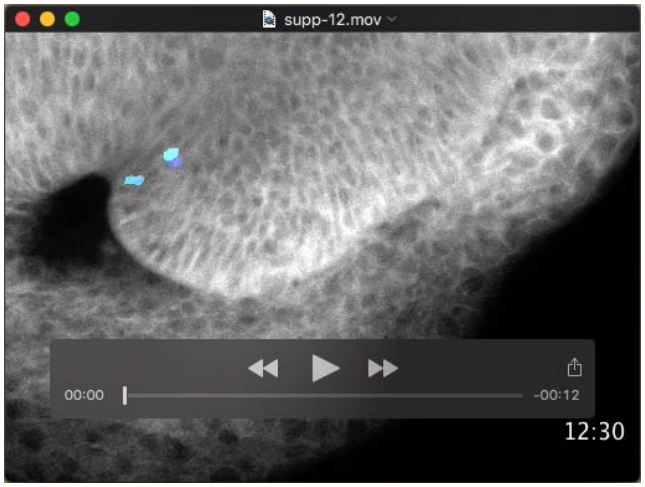

Movie 7. Related to Figure 2. *tfap2a;foxd3* double mutant nasal RPE nuclear trajectories from 12.5-24 hpf. Representative trajectories over membrane channel average (grayscale). ΔT between z-stacks, 2 minutes 30 seconds.

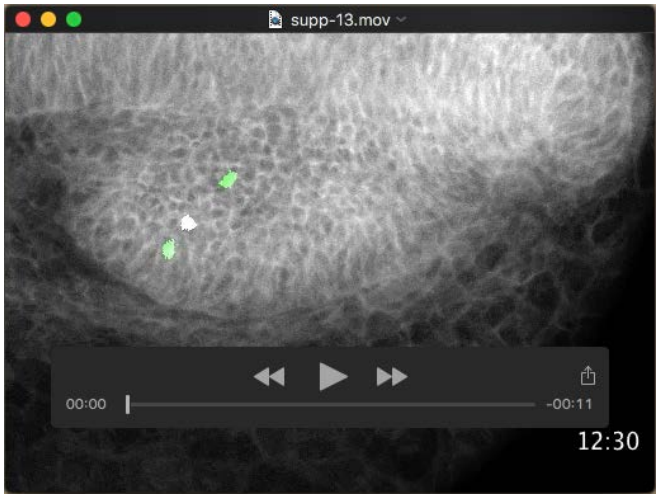

Movie 8. Related to Figure 2. Wildtype temporal retina nuclear trajectories from 12.5-24 hpf. Representative trajectories over membrane channel average (grayscale). ΔT between z-stacks, 2 minutes 45 seconds.

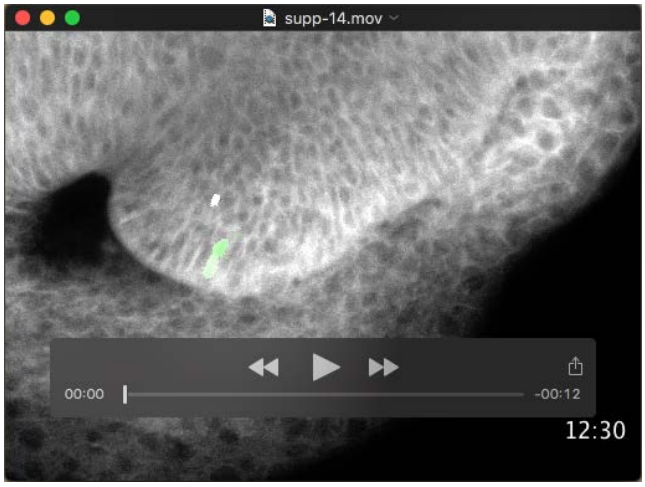

Movie 9. Related to Figure 2. *tfap2a;foxd3* double mutant temporal retina nuclear trajectories from 12.5-24 hpf. Representative trajectories over membrane channel average (grayscale). ΔT between z-stacks, 2 minutes 30 seconds.

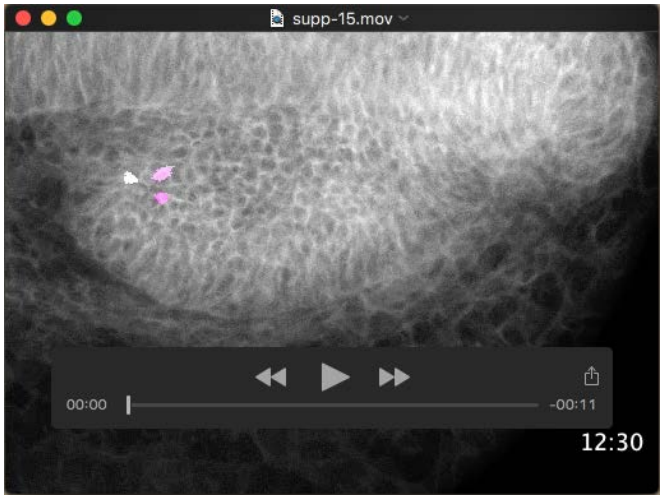

Movie 10. Related to Figure 2. Wildtype temporal RPE nuclear trajectories from 12.5-24 hpf. Representative trajectories over membrane channel average (grayscale). ΔT between z-stacks, 2 minutes 45 seconds.

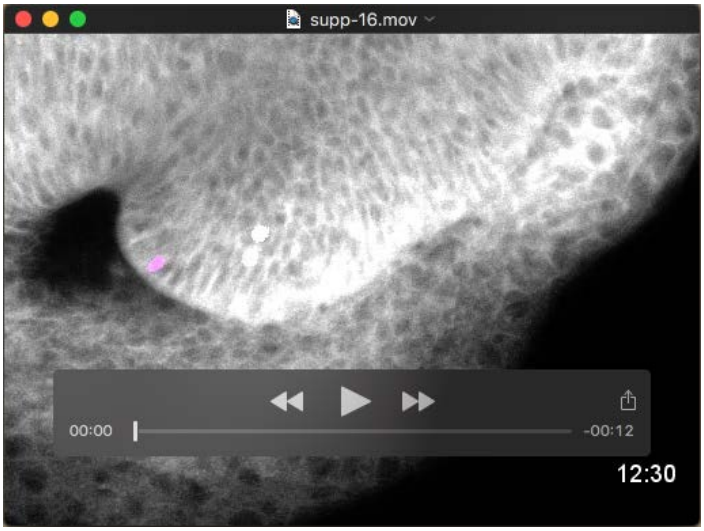

Movie 11. Related to Figure 2. *tfap2a;foxd3* double mutant temporal RPE nuclear trajectories from 12.5-24 hpf. Representative trajectories over membrane channel average (grayscale). ΔT between z-stacks, 2 minutes 30 seconds.